CZECH TECHNICAL UNIVERSITY IN PRAGUE

Faculty of Nuclear Sciences and Physical Engineering

Department of Physics

Bachelor thesis

Study of jet production at RHIC

Martin Kocmánek

Supervisor: RNDr. Jana Bielčíková, Ph.D.

Prague, 2015

ČESKÉ VYSOKÉ UČENÍ TECHNICKÉ
V PRAZE
Fakulta Jaderná a Fyzikálně Inženýrská
Katedra Fyziky

Bakalářská práce

Studium produkce jetů na urychlovači RHIC

Martin Kocmánek

Supervisor: RNDr. Jana Bielčíková, Ph.D.

Praha, 2015

Prohlášení:

Prohlašuji, že jsem svou bakalářskou práci vypracoval samostatně a použil jsem pouze podklady (literaturu, software, atd.) uvedené v přiloženém seznamu.

Nemám závažný důvod proti užití tohoto školního díla ve smyslu 60 Zákona .121/2000 Sb., o právu autorském, o právech souvisejících s právem autorským a o změně některých zákonů (autorský zákon).

V Praze dne

Title:
Study of jet production at RHIC

Author: Martin Kocmánek

Specialization: Experimental nuclear physics

Sort of project: Bachelor thesis

Supervisor: RNDr. Jana Bielčíková, Ph.D.

Abstract: Many experiments of present particle physics focus on research of a new state of strongly interacting medium called quark-gluon plasma (QGP). It is an extremely hot and dense nuclear matter consisting of free quarks and gluons, which are under normal condition confined in hadrons. QGP is created and studied in ultra-relativistic heavy-ion collisions which allow to reach extreme conditions. During early stages of a collision, partons of incoming nuclei undergo fragmentation and hadronisation which results in jets, collimated sprays of particles. Jets are an important probe of the QGP and study of their modification in medium provides information about properties of the medium. Jet-finding algorithms are used for jet reconstruction and their main goal is to cluster a set of particles measured by detectors into jets. The main aim of this bachelor thesis is to give a brief introduction to jet physics and overview of various jet algorithms and techniques in jet analysis. The thesis summarizes the recent results of jet analysis measured mainly by the STAR experiment at RHIC. This work also serves as my preparation for further analysis of jets in nucleus-nucleus collisions at RHIC.

Key words: quark-gluon plasma, nucleus-nucleus collisions, jet, jet algorithm, STAR

Názov práce:
Studium produkce jetů na urychlovači RHIC

Autor: Martin Kocmánek

Abstrakt: Veľa súčasných experimentov časticovej fyziky sa zameriava na výskum novej formy silne interagujúceho média nazvaného kvark-gluónová plazma (QGP). Kvark-gluónová plazma je veľmi horúca a hustá jadrová hmota pozostávajúca z voľných kvarkov a gluónov, ktoré sú za normálnych podmienok viazané v hadrónoch. QGP je vytvorená a študovaná v ultrarelativistických ťažko-iontových zrážkach, ktoré nám umožňujú vytvoriť spomínané extrémne podmienky. Počas počiatočných štádií zrážky partóny nachádzajúce sa v zrážaných jadrách podstúpia proces fragmentácie a hadronizácie, čo vedie k vytvoreniu jetov, kolimovaných spŕšok častíc. Jety sú dôležité sondy QGP a štúdium ich modifikácií v médiu nám poskytuje informácie o vlastnostiach vytvoreného média. Jety sú rekonštruované pomocou jetových algoritmov, ktorých cieľom je spojiť skupinu častíc nameraných detektorom do jetov. Hlavným cieľom tejto bakalárskej práce je poskytnúť úvod do jetovej fyziky, prehľad rôznych jetových algoritmov a spôsobov analýzy jetov. Zhŕňa niektoré nedávne výsledky analýzy jetov uskutočnených predovšetkým na experimente STAR na urýchľovači RHIC. Táto práca taktiež slúži ako moja príprava pre budúcu analýzu jetov v jadro-jadrových zrážkach na RHICu.

Kľúčové slová: kvark-gluonová plazma, jadro-jadrové zrážky, jet, jetový algoritmus, STAR

Acknowledgement

I am very grateful to my supervisor RNDr. Jana Bielčíková, Ph.D. for her willingness, patience, support, professional guidance, advices, language corrections and help with this bachelor thesis. Also I would like to thank to Jan Rusňák for his advices, suggestions and introducing me into jet analysis. And finally, I am grateful to all who supported me, especially my family and friends.

Contents

List of Figures

Chapter 1

Introduction to particle physics

Nowadays high energy physics is a connection of two fields: nuclear and particle physics that is also called physics of elementary particles. Both are a part of modern physics that was developed from the beginning of the 20th century. The main reason, why scientists are interested in this field of physics is long-lasting effort to understand and know the basic structure of matter. The present fundamental of nuclear physics is the Standard model that embodies a unified complex of theoretical knowledge and all known elementary particles. It is able to describe three from four fundamental interactions except gravitational: weak, strong and electromagnetic. It also includes relativistic quantum mechanics. The current formulation of the Standard model which includes the electroweak interaction was developed in 1970s by three physicists: Sheldon Glashow, Steven Weinberg and Abdus Salam. A theory that describes the strong interaction is Quantum Chromodynamics and it was developed also in 1970s by David Politzer, Frank Wilczek and David Gross.

1.1 Elementary particles

Fundamental constituents of matter are divided into several groups. The first division of particles is into fermions and bosons. Fermions are particles with half-integer spin 1/2 and obey Fermi statistics and Pauli principle. Leptons and quarks, which are elementary building blocks of matter are included in this group. Gauge bosons have an integer spin, follow Bose-Einstein statistics and do not obey Pauli principle. They are mediators of fundamental interactions.

Each particle can be characterized by its rest mass, electric charge and a group of quantum numbers: baryon and lepton number, spin... There are also antiparticles that have the same mass as their respective particle, but they have an opposite charge. In Figure 1.1 we can see division of particles according to the Standard model.

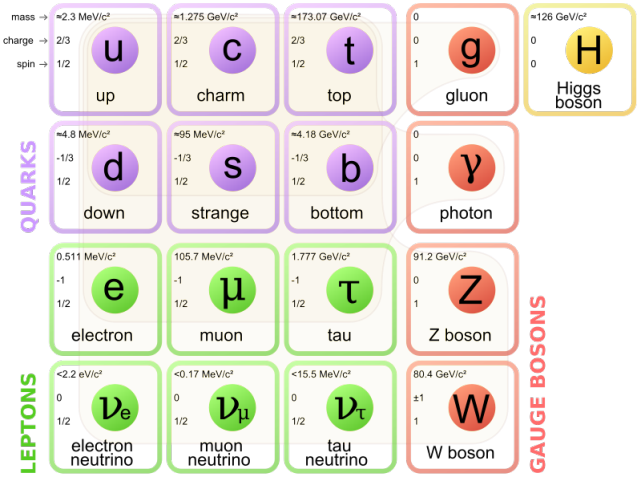

Figure 1.1: The Standard model of elementary particles [1].

Quarks and hadrons

A quark is a fundamental constituent of matter. According to the Standard model there are 6 quarks and their respective antiquarks classified to doublets in 3 generations. Their main characteristics is flavor and they are only particles which experience all four fundamental interactions. Quarks are denoted: up, down, strange, charm, top, bottom (2 in one generation), but only up and down are stable, quarks from the second and third generation decay quickly. To each flavor exists a quantity that has to be conserved in both strong and electromagnetic interactions. It is: strangeness S, charm C, beauty B and truth T. Quark can carry one of three colors which can be for illustration denoted as: red, green, blue (or specific anticolor). Quarks are constituent particles from which composite particles (hadrons) are formed. Hadrons are divided into two groups considering number of constituents: mesons consisting of a pair of quark-antiquark (pion $\pi^+ - u\bar{d}$) and baryons consisting of three quarks (proton uud). Hadrons are color neutral.

Leptons

Lepton is a particle that does not interact via the strong interaction. There are three lepton generations. Each generation consists of one negative charged lepton and relevant neutrino that does not carry any charge. Leptons are electron, muon and tau and their relevant neutrinos. To each generation is assigned a lepton number L_e, L_μ, L_τ which has to be conserved in all reactions.

Gauge Bosons

Gauge bosons are carriers of force and mediate fundamental interactions. They have an integer spin. The Standard model recognizes several kinds of gauge bosons: photons, W and Z bosons and gluons. Photons are associated with the electromagnetic interaction. W and Z bosons are carriers of the weak interaction. Gluons mediate the strong interaction. In addition, there is also the last discovered boson - Higgs boson. It explains why elementary particles have mass. Apart form these bosons,

gravitational force is supposed to be mediated by a hypothetically predicted graviton with spin 2, which has not been observed yet.

1.2 Fundamental interactions

As was said in the previous section, there are four basic interactions: electromagnetic, weak, strong and gravitational. These interactions and their properties are listed in Table 1.1. Their relative strength is expressed by a coupling constant α.

Interaction	Mediator	Range [m]	Relative strength
Strong	gluon	10^{-15}	1
Weak	W, Z boson	10^{-18}	10^{-12}
Electromagnetic	photon	∞	10^{-7}
Gravitational	graviton	∞	10^{-39}

Table 1.1: A comparison of four fundamental interactions. There are listed mediators of each interaction, its maximum range and the relative strength with respect to the strong interaction.

Electromagnetic interaction
Mediators of the electromagnetic interaction are photons that are massless and electrically neutral and do not interact with other photons. Energy of the photon depends on its wavelength. The electromagnetic force is well described by the theory of Quantum Electrodynamics. It acts on all electrically charged particles and has infinite range.

Weak interaction
Weak force is mediated by three heavy bosons. Two of them are electrically charged, each with opposite charge: W^+, W^- and with a mass $m_{W^\pm} = 80.4$ GeV/c^2. The third one is neutral, denoted Z_0 with mass $m_{Z_0} = 91.2$ GeV/c^2. Due to their large mass the range of the weak interaction is only 10^{-18} m. The weak interaction acts on all quarks and leptons and quarks can change their flavor. It is also responsible for the β decay.

Strong interaction
As the name indicates, the strong interaction is the strongest among all four fundamental forces and it is responsible for binding quarks in hadrons and also protons and neutron in nucleus. Its range is limited to the size of nucleus. The strong interaction will be described within the Quantum Chromodynamics in the next section.

Gravitational interaction
Gravity is the weakest interaction among forces mentioned above, therefore it is often neglected. It is the only interaction that is not included in the Standard model. It acts on all particles with a mass and has an infinite range.

1.3 QCD

Quantum chromodynamics (QCD) is a theory that describes the strong force, a fundamental interaction between partons: quarks and gluons. The strong force keeps quarks tightly bound in hadrons by means of gauge bosons - gluons. QCD explains a lot about dynamics and behavior of quarks and gluons in matter and it is an important part of the Standard model. There is a parallel with Quantum Electrodynamics (QED) describing the electromagnetic interaction. In QED the key property is an electric charge, which is analogous to the color charge in QCD. The color charge is carried by all fundamental particles of the strong interaction. There are three color charges which can be for simplicity denoted e.g.: red, green and blue and their anticolors that a quark can carry, while gluons can exist in 8 states. In QCD, the gluon is a force carrier of the strong interaction, carries a color charge and is able to interact with other gluons contrary to QED, in which a photon is a force mediator and does not carry any electric charge [2]. The strength of the strong interaction in comparison to the electromagnetic force with a coupling constant α is expressed by the coupling constant of the strong interaction α_s that is depicted in Figure 1.2. There are two important properties that are characteristic to the strong interaction:

- Asymptotic freedom - The coupling constant of QCD α_S depends on space distance, respectively is a function of the transfered transverse momentum q^2. If quarks are getting closer to each other ($\ll$ 1 fm) or transverse momentum of two colliding quarks is large, the amount of color force is decreasing. It means that quarks behave almost as free particles. A medium that consists of asymptotically free quarks and gluons is called quark-gluon plasma.

- Color confinement - The $V(r)$ potential of color field of quarks and antiquarks is a function of r which is defined as a distance between a quark and an antiquark. The $V(r)$ potential can be expressed by

$$V(r) = -\frac{4}{3}\frac{\alpha_s}{r} + kr \tag{1.1}$$

  where α_s is the coupling constant, k is a string tension and it is an empirical value which represents the strength of quark confinement force. This formula shows, that it is almost impossible to recede quarks on large distances. In comparison to electromagnetic or gravitational interaction, in which potential of coupling between electric or mass object is decreasing with larger distance, in strong interaction it is opposite. Potential energy of quarks is increasing with their larger mutual distance till the moment when it is large enough and the potential energy between them is sufficient for creating another quark-antiquark pair. This mechanism is schematically depicted in Figure 1.3. From one meson become two or more. The consequence that is responsible for impossibility to observe free quarks in vacuum is referred to as a quark confinement.

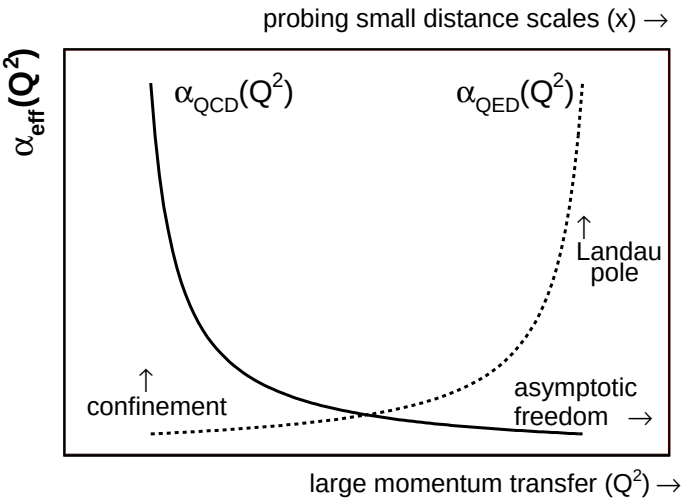

Figure 1.2: The coupling constants of QED and QCD [3].

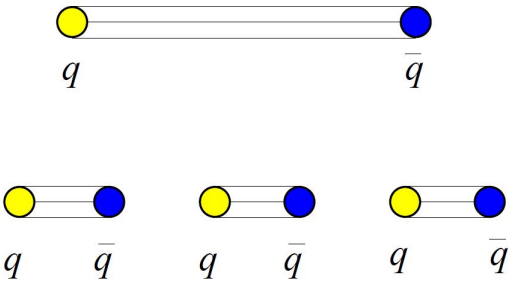

Figure 1.3: A schematic view of the confinement mechanism. The separating $q\bar{q}$ pair stretches a color string until the increasing potential energy is sufficient to create another $q\bar{q}$ pair. More pairs may be produced in this way, which leads to the formation of final state hadrons [4].

Chapter 2

Physics of high energy nucleus collisions

2.1 Quark-gluon plasma

In modern nuclear particle physics, many experiments focus on the research of nuclear matter, called quark-gluon plasma (QGP). The quark-gluon plasma is a new state of hot and dense nuclear matter consisting of free partons - quarks and gluons. It is theoretically predicted by the asymptotic freedom concept from the QCD theory which was described in the previous chapter. QGP exists only at extreme high temperature T_C and baryonic density μ_B in the order of 10^{12} K and 10^{12} kg.cm^{-1} [5], when quarks and gluons are deconfined. Considering these conditions, QGP can be found in three places: in the first microseconds after the Big Bang, in the center of compact stars and finally at the initial stage of colliding heavy nuclei at relativistic energies.

In this work, we focus on QPG formed in heavy-ion collisions and discuss its signatures. The relativistic heavy-ion collision is a dynamic process, where QGP is formed in an initial stage of the collision. To study the properties of QGP it is necessary to know and have devices to create it, because the typical time scale and size are of the order of 10 fm and 10 fm/c. For this purpose, particle accelerators are used, which are usually two circular pipes, where beams of nuclei circulate in an opposite direction and collide on a specific place in the accelerator. This collision or more precisely its products are measured by large detectors in order to study structure of matter. Nuclei are accelerated in colliders close to the velocity of light c (3.10^8 m.s^{-1}) and due to the Lorentz contraction in longitudinal direction along the beam axis they are not spherical, but resemble a thin disc. When the nuclei collide, they pass through each other and create a fireball of hot and dense nuclear matter. Immediately after the collision, the fireball starts to expand. Due to elliptical shape of the collision region, the pressure gradients are oriented preferentially along the beam axis. This results in a large anisotropic asymmetry of produced particles, commonly referred to as flow.

In Figure 2.1 we can see the phase diagram of nuclear matter that is still one of

the main subject of current research. The horizontal axis represents baryon chemical potential μ_B and the vertical axis is temperature T. When T and μ_B is low the matter is in a state of hadron gas. By increasing T or μ_B hadron gas transforms to QGP, where the white curve symbolizes the first order transition. This curve ends at a specific point, referred to as a critical point. From this point the crossover region starts, where the phase transition of the second order occurs. The critical point is explored by a dedicated Beam Energy Scan (BES) program at RHIC.

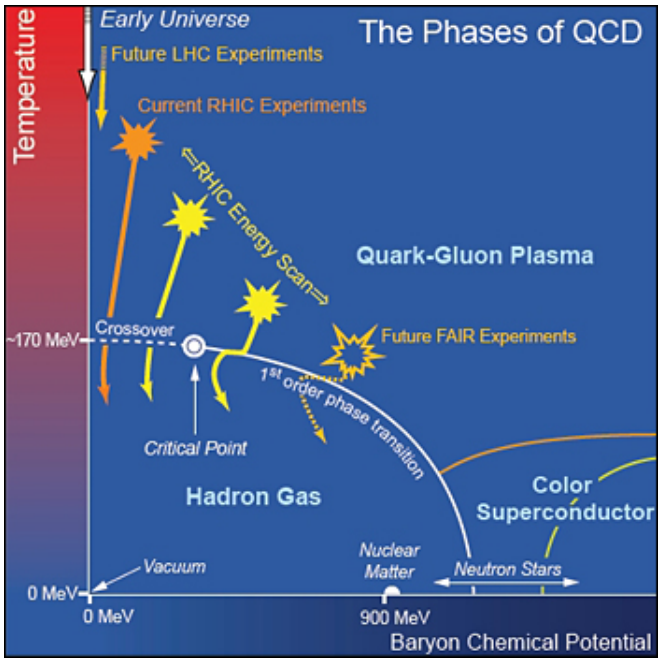

Figure 2.1: A schematic QCD phase diagram of nuclear matter [6].

2.2 Basic kinematic observables

Particles participating in a nuclear collision are accelerated to very high velocities that are comparable to the velocity of light. Thus for description of their kinematic properties it is useful to define several variables accounting for relativistic effects. These variables remain invariant in transition from one frame to another.

One of them is a transverse momentum p_T. Particles move along axis z in their system and that results in Lorentz contraction in the direction of z. The component of momentum parallel to the z axis is longitudinal momentum $p_{||} = p_z$. Components p_x and p_y of the momentum four-vector $P = (E/c, p_x, p_y, p_z)$, where E is the energy and $\vec{p} = (p_x, p_y, p_z)$ momentum of particle remain without change. p_T is then defined as

$$p_T = \sqrt{p_x^2 + p_y^2} = p \sin\theta. \tag{2.1}$$

For description of a position of detected particle, spherical coordinate system with azimuthal and polar angle is used. The azimuthal angle ϕ is an angle between the track of the particle and the plane that is perpendicular to the direction of

colliding nuclei. The polar angle θ is an angle between the beam axis and the direction of the particle.

The next variable is rapidity that is a measure of velocity. It is defined as

$$y = \frac{1}{2} \ln \left(\frac{E + p_z}{E - p_z} \right). \tag{2.2}$$

The rapidity of the light is infinity while velocity is limited by a finite value. The rapidity is an additive quantity contrary to velocity that is not additive.

In the high energy physics, for the measure of the angle between the beam axis and momentum of a particle, the pseudorapidity is usually used instead of the polar angle. The pseudorapidity η is defined as the function of the polar angle:

$$\eta = -\ln \tan \theta/2, \tag{2.3}$$

where $\theta = \arccos \frac{p_z}{p}$. It is possible to show that rapidity equals the pseudorapidity when energy of the particle is very high with respect to its mass: $p \gg m$. The relation between the pseudorapidity and polar angle is depicted in Figure 2.2

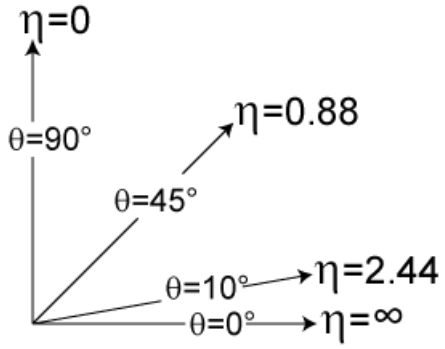

Figure 2.2: Relation between the pseudorapidity η and polar angle θ [7].

The energy of the nuclear collision is usually expressed by a center of mass (CMS) energy $\sqrt{s}$ or a center of mass energy per nucleon $\sqrt{s_{NN}}$. In case of a symmetric collision, the relation between previously defined CMS energies is $\sqrt{s_{NN}} = \sqrt{s}/A$, where A is a nucleon number. The center of mass energy of two colliding nuclei with momenta p_1, p_2 and energies E_1, E_2 is:

$$\sqrt{s} = \sqrt{(E_1 + E_2)^2 - (p_1 + p_2)^2} \tag{2.4}$$

In general when collisions are studied we can distinguish different kinds of events. The first one is a minimum bias event. Minimum bias events are all events measured without application of any selection criteria. Beside that there are events which are chosen or removed based on a certain selection criteria. These criteria are used by a trigger that decides if an event should be recorded for later analysis or not. The trigger is a system that searches for events in which we are interested. It is used for selection of the type of collisions or particles, whose production is rare.

2.3 Geometry of nuclear collision

One of the most important parameters for description of a collision is an impact parameter b that has a value from 0 to $R_1 + R_2$ [8], where R_1 and R_2 are radii of the colliding nuclei. It represents the minimal distance between centers of interacting nuclei in the transverse plane. If the impact parameter increases, distance between nuclei is also larger. Centrality is a quantity which relates to the impact parameter. According to the value of the impact parameter, collisions can be categorized to distant ($b > 2R$, where R is a radius of nucleus), peripheral ($b < 2R$) and central ($b \approx 0$). Moreover, collisions between peripheral and central can be divided into two groups: semi-central and semi-peripheral. Figure 2.3 illustrates three basic types of a collision: (a) is a distant collision, (b) is a peripheral collision and (c) is a central collision. As the impact parameter decreases, colliding bunches of nuclei overlap more and consequently more nucleus-nucleus collisions happen. If a nucleon is involved in a collision, it collides with another nucleon and is referred to as a participant. Nucleons, which do not participate in the collision are referred to as spectators. The alternative definition of centrality and its relation to other variables is illustrated in Figure 2.4. Centrality is connected with centrality classes that are defined as percentile of the total geometric cross section or distribution of types collisions in the event according to the impact parameter. Basic centrality classes, which are also depicted in Figure 2.4 are: 0-5% (the most central), 5-10% (semi-central), 10-20%, 20-30%(semi-peripheral), 30-50% (peripheral).

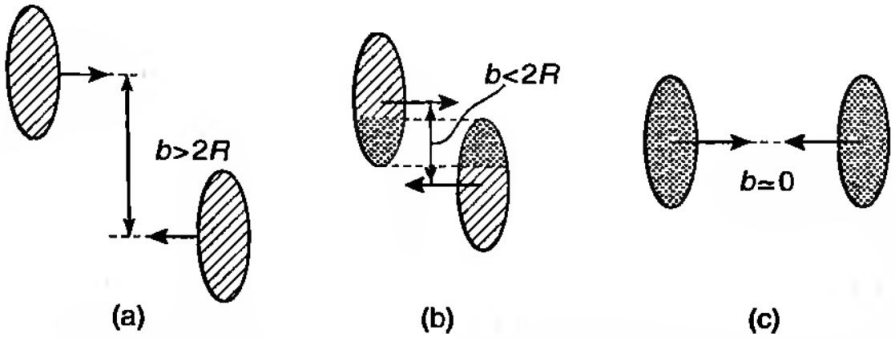

Figure 2.3: Geometry of a nuclear collision according to the value of the impact parameter: (a) - distant collision, (b) - peripheral collision and (c) - central collision. [5]

After the collision spectators continue in the longitudinal direction, meanwhile in the region of fireball there are mutual collisions between interacting particles, which can result in QGP and production of new particles.

The next variable, which can be used for description of the collision is multiplicity. It is a total number of produced particles and it is closely related to the centrality. In case of the nucleus-nucleus collision when the impact parameter is decreasing, more nucleons interact among themselves and more particles are produced, which means that multiplicity is higher. Moreover multiplicity is proportional to the energy released in the collision, if the energy of collision is higher then also multiplicity increases.

Geometry of a heavy-ion collision and its quantities, for example the impact parameter, cannot be measured directly in the experiment. Therefore the impact parameter is determined indirectly from the particle multiplicity, transverse energy or the number of spectator nucleons (measured by "zero-degree calorimeter" ZDC) [9]. The number of participant nucleons N_{part} in the collision can be evaluated by the Glauber model [5] described bellow.

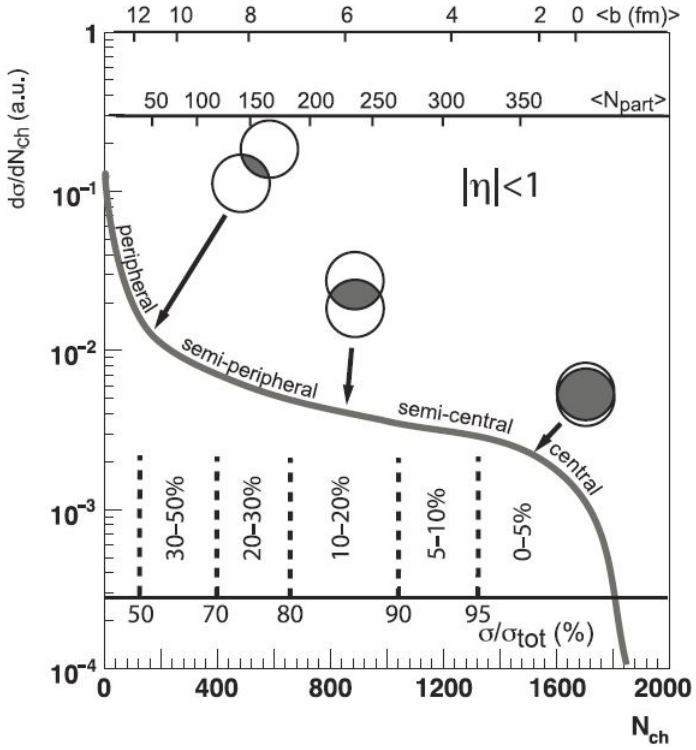

Figure 2.4: Dependence of cross section on number of produced charged particles N_{ch}. The graph also depicts the centrality definition from the final-state particle multiplicity and its correlation with the the impact parameter b, the number of participating nucleons N_{part} in the collision, centrality classes and the ratio of cross section σ in the most central collision to total cross section σ_{tot} of produced particles [10].

2.3.1 Glauber model

The Glauber model is used for description of a high-energy heavy-ion collision and calculation of basic geometric quantities of the collision such as the number of participant nucleons N_{part} and binary nucleon-nucleon collisions N_{coll} [11] and also the total cross section of a reaction. The Glauber model has two assumptions. The first is that nucleons travel in straight lines without any deflection after the collision. According to this, the Glauber model is a good approximation at very high energies. Secondly, inelastic cross section σ_{NN}^{in} of the nucleon-nucleon collision

is the same as in the vacuum. It means that secondary particle production and excitation of nucleons are not taken into account. A collision is treated as multiple nucleon-nucleon interactions. The geometry of the Glauber model is shown in Figure 2.5. N_{part} and N_{coll} is computed by the Glauber model as follows [5]:

$$N_{part}(b) = \int d^2s\, T_A(s) \left(1 - e^{-\sigma^{in}_{NN} T_B(s)}\right) + \int d^2s\, T_B(s-b) \left(1 - e^{-\sigma^{in}_{NN} T_A(s)}\right) \quad (2.5)$$

$$N_{coll}(b) = \int d^2s\, \sigma^{in}_{NN} T_A(s) T_B(s-b) \quad (2.6)$$

where T_A is the thickness function defined as $T_A(s) = \int dz \rho_A(z,s)$, z is an axis, b is the impact parameter, s is a distance in Figure 2.5, σ^{in}_{NN} inelastic cross section and ρ is the nuclear mass number density ussually given by Wood-Saxon parametrization and normalized to the mass number A. The average N_{part} for a p+p collision is 2, for a p+A collision $N_{part} = N_{coll}+1$ and for an A+A collision $N_{part} = 2A$.

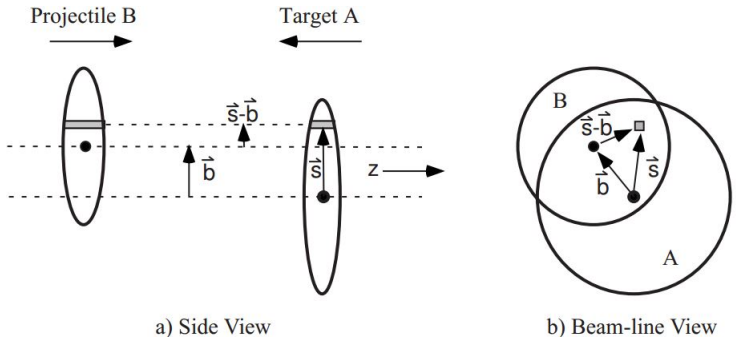

Figure 2.5: A schematic representation of the Glauber model geometry with longitudinal (a) and transverse (b) views [11].

2.4 Space-time evolution of nuclear collision

Medium that is created in an ultra-relativistic heavy-ion collision from the beginning to the time of detection particles undergoes several different phases during its evolution. The space-time evolution of the initial to final stage is depicted in Figure 2.6.

Immediately after the collision (in the order of femtoseconds) the region of a fireball goes through three main phases: pre-equilibrium and thermalization, hydrodynamical evolution and freeze -out and post-equilibrium [5] Processes in these phases are not completely understood yet and they are the main interest in current research to describe and adequately explain them in theoretical way. The evolution of a nuclear collision is described with the increasing time τ as follows

- $0 < \tau < \tau_0$
  The time 0 expresses the moment of a collision, when a large amount of energy

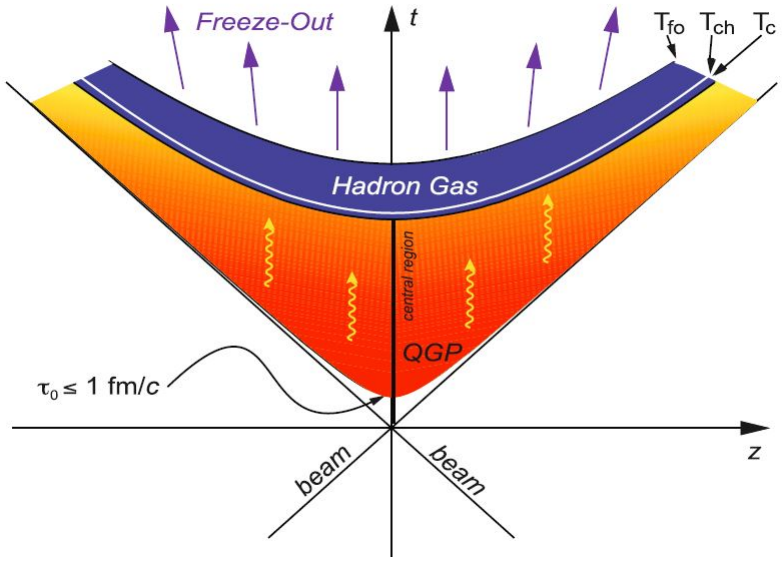

Figure 2.6: Space time evolution of a nuclear collision [6].

of two colliding nuclei is released. As was mentioned before the hot and dense medium of nuclear matter called fireball is immediately formed. The stage of pre-equilibrium is achieved, when the partons are created. This system tends to the state of thermal equilibrium, which cause its fast expansion, when the temperature and pressure are decreasing. At the time τ_0 the system reaches thermal equilibrium and the time of this process is estimated to be about $\tau = 1$ fm/c.

- $\tau_0 < \tau < \tau_f$
  If thermalization is fast enough, then hot and dense nuclear matter, eventually QGP is formed, which is in a state of local equilibrium. By the stage of thermal equilibrium, the medium behaves as an ideal liquid and the theory of relativistic hydrodynamics can be used for describing this stage and its subsequent progress. After some time of progress of the medium the process of hadronization begins.

- $\tau = \tau_f$
  Free quarks and gluons start to confine to hadrons. It happens at the time of τ_f, when the temperature of QGP falls to the critical value T_c. This effect is also called freeze-out and phase transition between QGP and hadronic matter occurs. But there are two kinds of freeze-out: the chemical and thermal which is also called kinetical freeze-out. The first comes chemical freeze-out and its temperature is higher than of the thermal freeze-out. During chemical freeze-out particles undergo mutual elastic collisions until the thermal freeze-out comes. In this phase, new particles are not produced anymore. A number of particles stabilizes at certain equilibrium with a constant baryochemic potential and temperature. Finally, when the thermal freeze-out takes place, particles start to fly away from the region of the collision, because the mean

free path is almost identical to the size of the system.

- $\tau_f < \tau$
  After time τ_f decoupling starts, particles recede each other and leave region of the collision.

All individual stages of the relativistic heavy ion collision are schematically depicted in Figure 2.7.

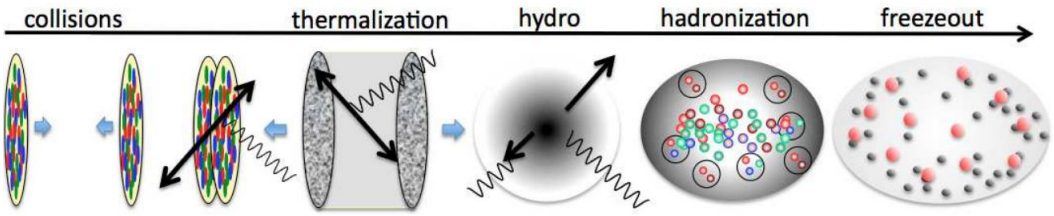

Figure 2.7: Evolution of a heavy ion collision [12].

2.5 Probes of QGP

In a high energy ion collision might be created QGP and the probability of its creation depends proportionally on the center mass energy of colliding ions and centrality. For probing the presence of QGP and its properties we need to have sensitive probes. The state of a quark gluon plasma created during the collision lasts for a very short time - in the order of tens of fm/c and for this reason its direct observation is really difficult, because only hadrons and leptons in final state are observable. Thus it is necessary to find out probes and methods for studying QGP indirectly. Particles that arise from the collision carry important information about properties of QGP and they represent indirect indication of deconfined phase of matter. In this section some of the probes of QGP are mentioned and briefly explained for example elliptic flow, suppression of particles with high p_T described by nuclear modification factor R_{AA} and jet quenching. There are also another probes of QGP: direct photons, dileptons, strangeness enhancement or quarkonium suppression, which we do not discuss here and refer reader to e.g. [9] or [13].

2.5.1 Elliptic flow

When a collision is non-central, the overlap region of nuclei has an ellipsoidal shape. The geometry anisotropy of the primordial interacting zone results in imbalanced pressure gradients and thus collective anisotropic azimuthal emission of hadrons in a plane in the beam direction [9]. This is referred to as an elliptic flow. According to hydrodynamics pressure gradients are the largest in the direction of the reaction plane and the system will expand mainly in this direction. The largest elliptic flow is measured in non-central collisions and the lowest in central collisions in which there is no asymmetry [5].

Elliptic flow can be expressed mathematically by a parameter v_2 that is derived from a Fourier expansion of hadron production depending on azimuthal angle ϕ to the plane of the collision ψ_r as:

$$E\frac{d^3N}{d^3p} = \frac{d^2N}{2\pi p_T dp_T dy}\left(1 + \sum_{n=1}^{\inf} 2v_n \cos[n(\phi - \psi_r)]\right) \tag{2.7}$$

where E is energy, p momentum, p_T transverse momentum, ϕ azimuthal angle, y rapidity of a particle and ψ_r angle of direction to event plane. The coefficients v_n in the Fourier expansion are calculated by:

$$v_n(p_T, y) = \langle \cos\left[n(\phi - \psi_r)\right] \rangle \,. \tag{2.8}$$

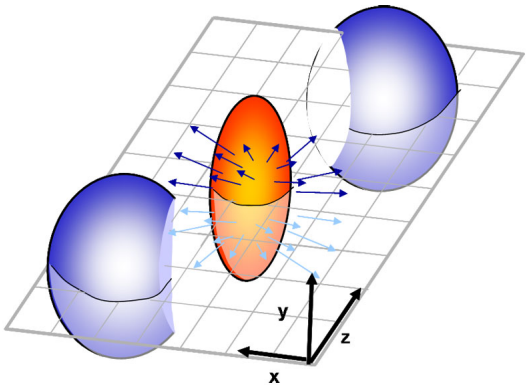

Figure 2.8: A schematic view of the collision zone of two incoming nuclei [14].

2.5.2 Nuclear Modification Factor

For probing properties of QGP particles with high transverse momentum $p_T > 2$ GeV/c are used. These particles result from hard parton scattering in the initial stage of the collision. Meanwhile particles with $p_T < 2$ GeV/c are produced in all stages of the collision. High p_T particles traversing dense medium can be suppressed because they lose energy by two effects. The dominant energy loss is caused by medium-induced gluon radiation. Secondly partons lose energy due to elastic collision with medium. Increased energy density of medium causes larger energy loss of partons.

A nuclear modification factor is a convenient tool for probing of QGP quantitatively by studying and comparing yields of high p_T hadrons in different types of collisions. It is defined as a ratio of yields in a nucleus collision to a p+p collision. The nuclear modification factor compares a p_T differential yield in a heavy-ion collision to the differential production cross section in a p+p collision at the same CMS energy $\sqrt{s_{NN}}$. This ratio is expressed by the following formula:

$$R_{AA}(b, y, p_T) = \frac{1}{\langle T_{AA}(b) \rangle} \frac{\mathrm{d}^2 N_{AA}/\mathrm{d}y\mathrm{d}p_T}{\mathrm{d}^2 N_{pp}/\mathrm{d}y\mathrm{d}p_T} \tag{2.9}$$

T_{AA} is a nuclear overlap function that accounts for the increased parton flux in A+A collisions compared to p+p collisions and it is related to the number of binary nucleon-nucleon collision N_{coll} that are calculated by the Glauber model [15].

If the nuclear modification factor is equal to 1, then there is not difference in yields in p+p and A+A. We do not observe influence of medium on particle production. In the case when $R_{AA} < 1$ it is referred to as a suppression when the number of particles produced in A+A collision is smaller than in p+p and contrary to previous case there is expectation of QGP existence. When $R_{AA} > 1$ it denotes enhancement in particle production, known as Cronin enhancement. The main source of enhancement hadron production at intermediate p_T range is mainly partonic scattering at the initial impact and multiple interactions in nuclear matter [16]. Comparison of yields between d+Au and A+A collision can be seen in Figure 2.10. In Au+Au collisions we can observe suppression, but in d+Au enhancement of particle production.

There is also a second possibility to describe influence of the medium on particle production. We can compare collisions with different impact parameters: central and peripheral collisions. For this purpose nuclear modification factor R_{CP} is defined:

$$R_{CP}(y, p_T) = \frac{\langle N_{coll,per} \rangle}{\langle N_{coll,cent} \rangle} \frac{\mathrm{d}^2 N_{per}/\mathrm{d}y\mathrm{d}p_T}{\mathrm{d}^2 N_{cent}/\mathrm{d}y\mathrm{d}p_T} \tag{2.10}$$

R_{CP} is usually used if data from p+p collisions are not at disposal at the same $\sqrt{s_{NN}}$ as A+A collision or they have too small statistics.

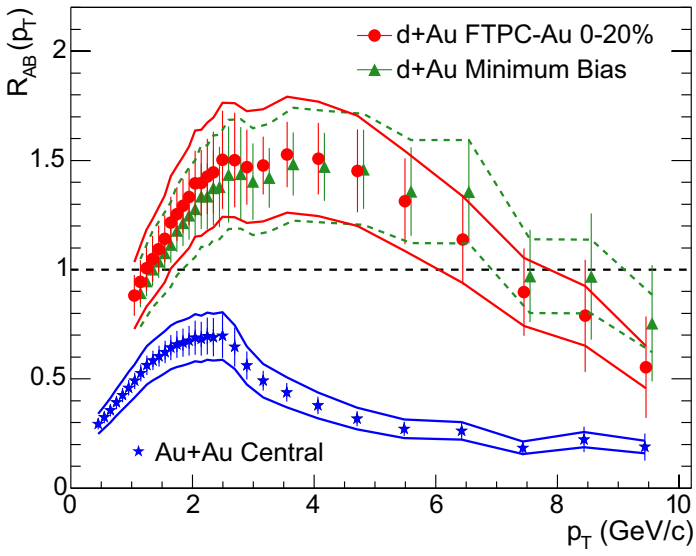

Figure 2.9: The nuclear modification factor R_{AB} for minimum bias and central d+Au collisions, and central Au+Au collisions measured by the STAR experiment at RHIC [17].

2.5.3 Jet quenching

At the initial stage of a heavy-ion collision when hard scattering occurs, two partons can be created. They recoil, fragment and hadronise into back-to-back shower of hadrons, known as jets [18]. If the parton has a high initial transverse momentum p_T or mass, it is called a hard probe. On its trajectory to the detector it can pass through strongly interacting dense medium - QGP and lose energy. After subsequent hadronization the quantity of produced particles might be lesser due to the energy loss and it might cause modification of the spectrum of jets and their properties. This phenomenon is referred to as a jet quenching. The first evidence of jet quenching has been observed in $\sqrt{s_{NN}} = 200$ GeV Au+Au collisions at RHIC [19] and later at the LHC [20]. This phenomenon will be discussed later in more details. Jet quenching provides direct information on the QCD matter and its thermodynamical properties such as temperature, energy or particle densities and transport properties (viscosity, diffusivity and conductivity coefficients) that can be obtained by comparing the measurements of jets in nucleus-nucleus collisions to proton-proton collisions [21]. This phenomenon is depicted in Figure 2.10. On the left-hand side of the figure there is a di-jet event arising from the p+p collision, in which the dense and hot medium is not created contrary to the right figure, where the medium is created and jets are modified and quenched. In the pp collision the size of both opposite jets is almost the same, but in a heavy-ion collision, the size of a jet arising from the edge of the collision region is larger than size of the opposite jet that is suppressed by medium. We can see that not only presence of medium change the properties of a jet, but also the position of its emergence and quantity of medium.

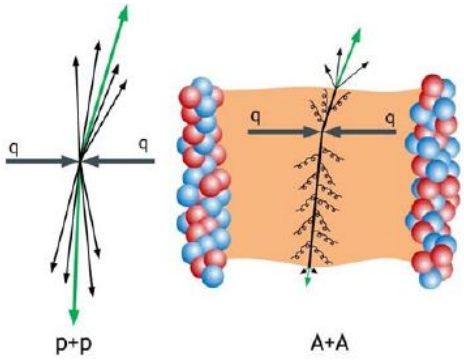

Figure 2.10: Jet quenching [22].

Chapter 3

STAR Experiment

3.1 RHIC

Relativistic Heavy Ion Collider (RHIC), shown in Figure 3.1, is the second largest collider in the world currently in operation. It is the first device capable of colliding heavy ions which began operation in 2000. In 2010 the Large Hadron Collider started its operation at the European Organization for Nuclear Research (CERN) in Geneva, where are also carried out experiments to explore QGP, but in higher energies than at RHIC. RHIC is located at Brookhaven National Laboratory (BNL) on the Long Island near New York. It was built in order to collide relativistic protons and heavy ions to study formation of quark-gluon plasma and spin physics by experiments with polarized protons. RHIC is able to collide various ion species, as well as is capable to study asymmetric collisions - beams with unequal masses. So far following systems were measured: p+p, d+Au, ^{3}He+Au, Au+Au, Cu+Cu and U+U. The maximum energy of beam for collisions of heavy nuclei is $\sqrt{s_{NN}} = 200$ GeV per nucleon pair and $\sqrt{s} = 500$ GeV for p+p collisions. For Beam energy scan are used different energies of the Au+Au collisions. The range of energy is from $\sqrt{s_{NN}} = 7.7$ to 39 GeV and with larger data set at 62, 130 and 200 GeV [23].

RHIC consists of two separated storage rings (beam lines) of superconducting magnets, that are 3.8 km long in circumference with six intersection points located on straight sections between 6 arc sections. The superconducting magnets include various types: dipoles, quadrupoles and sextupoles, that are utilized to bend, focus and steer the beams. The total number of magnets is 1740 and they are cooled to temperature of less than 4.6 K. For accelerating heavy ions to the maximum energy it is necessary to utilize accelerator complex. Firstly heavy ions are accelerated to energy of 1 MeV/nucleon by the Tandem Van de Graaff. Ions continue to the Booster Synchrotron, where are accelerated to 95 MeV/nucleon and then are delivered to the AGS and reach energy up to 10.8 GeV/nucleon. Finally they are injected to RHIC via Beam Transfer Line. Before each section, heavy ions are always partially stripped of electrons. Polarized protons start accelerating at 200 MeV Linac and then they undergo the same accelerating scheme as heavy ions [24]. Initially, RHIC was used for four independent experiments: BRAHMS, PHOBOS, PHENIX and STAR. BRAHMS and PHOBOS already successfully completed their experimental program and already only STAR and PHENIX are in operation.

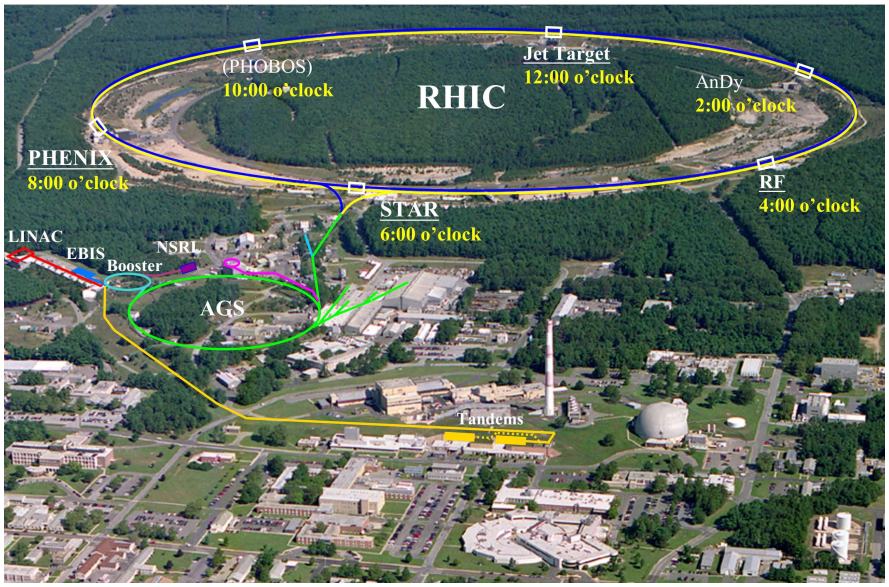

Figure 3.1: Relativistic Heavy Ion Collider [25].

3.2 STAR detector

The STAR detector [26] (Solenoidal Tracker at RHIC), depicted in Figure 3.2, was developed in order to study behavior and properties of strongly interacting QCD matter produced at high temperatures and energy densities in high energy heavy-ion collisions. It is able to observe and identify the majority of particles produced in a collision. The STAR detector is located at intersection point that is at the 6'o clock position of the RHIC collider. It has a shape of cylinder with detector layers around the beam axis. Most of the detectors are placed at mid-rapidity and have full azimuthal angle coverage. The STAR detector is 6.85 meters long and the radius is 7.32 meters. Around the whole detector is a large solenoidal magnet with magnetic field of 0.5 T. STAR consists of several types of specialized detectors and subsystems differing by the method of detecting particles. These detectors allow tracking and particle identification based on measurement of trajectory or deposited energy of particle. These detectors are: Time Projection Chamber (TPC), Time Of Flight detector (TOF), Barrel ElectroMagnetic Calorimeter (BEMC), Vertex Position Detector (VPD), Beam Beam Counter (BBC), Muon Telescope Detector (MTD), Heavy Flavor Tacker (HFT), Zero Degree Calorimeter (ZDC), Silicon Strip Detector (SSD) and others. The main purpose of the STAR experiment is to measure with large spatial acceptance hadrons, leptons and photons arising from proton-proton or heavy-ion collisions.

3.2.1 Time projection chamber

The Time projection chamber (TPC) [28] is the largest detector of STAR. Its function is mainly track reconstruction of charged particles on the basis of the measurement of energy loss and curvature of tracks in the magnetic field of 0.5 T parallel

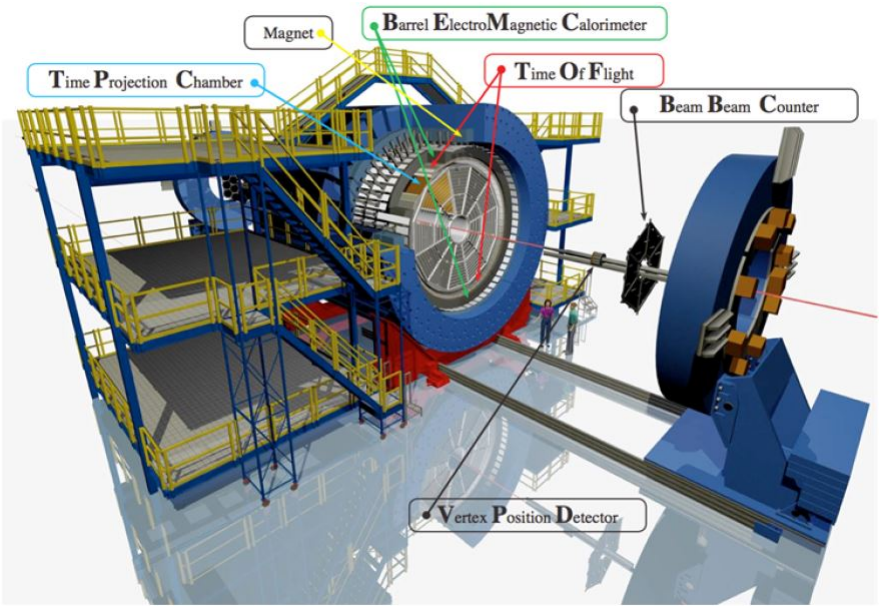

Figure 3.2: STAR detector [27].

to the beam pipe. The TPC has a cylindrical shape and length 4.2 meters, inner radius is 50 cm and outer radius is 200 cm. It covers full azimuthal angle 2π with pseudorapidity $|\eta| \leq 1$. The overall tracking efficiency of the TPC is 80-90% and the systematic error of track reconstruction is about 6%. It is filled with P10 gas regulated at the pressure of 2 mbar larger than atmospheric pressure. Gas P10 is a mixture of two gases: argon (90%) and methane (10%). In order to obtain good detection performance, gas should not influence yield or velocity of electrons. Inert gas does not decelerate electrons and does not capture them and organic gas prevents propagation of UV rays. But in the future it is planned to fill the TPC with a mixture of helium (50 %) and ethane (50%) to improve efficiency. The TPC consists of a central cathode and two anodes located at sides. The whole detector is divided into two parts, where in between is a thin carbon coated annulus membrane - High Voltage membrane with 28 kV. The function of this membrane is to form a uniform longitudinal electric field that is parallel to the beam pipe and its value is 135 V/cm. At both ends of the TPC there is a readout system based on multi-wire proportional chambers (MWPC). The end caps contain 12 sectors of anode pads. A scheme of the TPC is depicted in Figure 3.3.

A charged particle going through the TPC ionizes the gas around its track and releases electrons from gas molecules. These kicked out free electrons are accelerated in the electric field and drift with the constant velocity to the anode end caps. Before electrons reach end of the TPC, their velocity is increased by electric field to allow ionization of gas and produce another electrons. This effect is called avalanche. The average velocity of an electron is referred to as a drift velocity. The average number of produced electrons is proportional to the energy released in the detector (or energy that particle loses in the TPC). Then the signal of the electron is amplified and recorded. Wires of MWPC are formed into grid, which allows us to determine two

coordinates (x,y) of each part of a track. The longitudinal coordinate z is obtained from the time of drift. This means that the TPC is able to reconstruct tracks in 3 dimensions, therefore we can obtain important information about trajectory of each charged particle passing through the TPC.

To calculate energy loss of a particle in material, the Bethe-Bloch formula is used:

$$\frac{dE}{dx} = 4\pi N_A r_e^2 m_e c^2 z^2 \frac{Z}{A}\frac{1}{\beta^2}\left(\frac{1}{2}\ln\frac{2m_e c^2\beta^2\gamma^2 T_{max}}{I^2} - \beta^2 - \frac{\delta}{2}\right) \tag{3.1}$$

where N_A is the Avogadro number, r_e classical electron radius, m mass of particle that loses energy, c speed of light in vacuum, ρ density of material, Z proton number, A nucleon number, W_{max} maximum energy transfer in a single collision, I mean excitation energy and δ density correction. This formula allows us to identify particles as can be seen in Figure 3.4 where the $\frac{dE}{dx}$ is a function of momentum of particles measured by the STAR TPC. Momentum of particles is computed from a curvature of the particle track in the magnetic field.

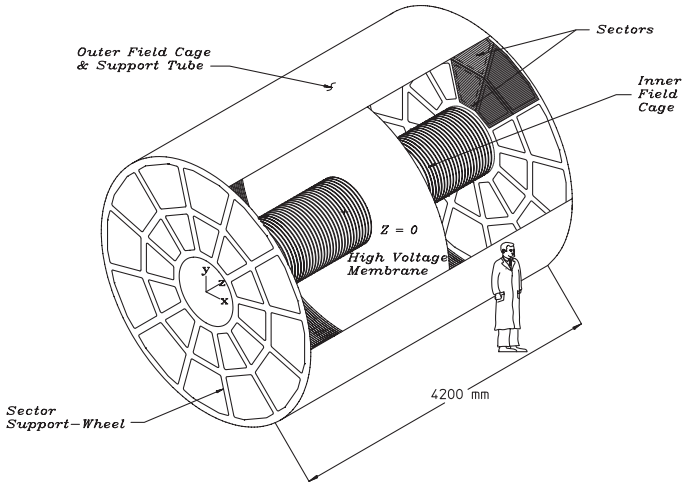

Figure 3.3: A schematic view of a Time Projection Chamber [28].

3.2.2 Time of flight

The Time of Flight detector (TOF) of STAR [24] is designed for improvement of direct identification of hadrons. It is located between the TPC and the BEMC and covers full azimuthal angle and pseudorapidity $|\eta| \leq 1$. The TOF is based on Multi-gap Resistive Plate Chamber (MRPC) technology. The MRPC module is in each tray and there are 120 trays included in the TOF. The TOF detector is activated by a VPD (Vertex position detector) and with assistance of momentum obtained from the TPC we can very precisely identify particles. The time resolution of the TOF is high - 100 ps and allows the TOF effectively distinguish electrons from heavier hadrons with a low momentum. Thus it is possible to identify pions

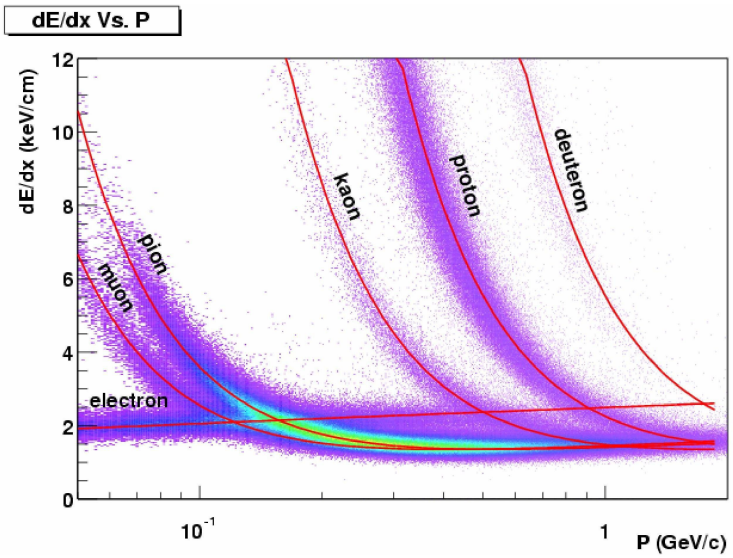

Figure 3.4: The result of energy loss dE/dx distribution measurement in TPC STAR as a function of the transverse momentum p_T. Measurement is used for particle identification [28].

and protons to 7-8 GeV/c, kaons to 3 GeV/c and electrons in the interval of 0.15 - 4 GeV/c [29]. High momentum particles are identified by other detectors, e.g. the BEMC. The principle of particle determination or respectively its mass is as follows: the time of flight particles traversing through detector is measured. The starting time t_0 is recorded by the VPD and the TOF measures the end time t_1. From these measurements we can obtain the time-of-flight interval $\Delta t = t_1 - t_0$. Then using the interval Δt and the length s of particle track acquired from the TPC, the value of inverse velocity is computed:

$$\frac{1}{\beta} = \frac{c\Delta t}{s}. \tag{3.2}$$

Finally from the momentum of the particle and its velocity β we are able to calculate mass according to the formula:

$$m = p\sqrt{\left(\frac{1}{\beta^2}\right)^2 - 1} \tag{3.3}$$

Measurements from the TOF detector help to improve identification of particles from the TPC.

3.2.3 Barrel Electromagnetic calorimeter

The STAR Barrel Electromagnetic Calorimeter (BEMC) [30] is located between the TOF detector and the solenoidal magnet. Its distance from the beam pipe is

223.5 cm. It covers full azimuthal angle and has pseudorapidity coverage $|\eta| \leq 1$. Its purpose is to measure energy deposition of high momentum particles such as photons, electrons and hadrons. The BEMC consists of 120 calorimetric modules (in azimuthal angle), each segmented into 40 towers (in pseudorapidity). A view of the BEMC module is illustrated on Figure 3.5. The total number of towers in the BEMC is 4800, where the effective size of the tower as the BEMC resolution is 0.05 x 0.05 = $\Delta\phi$ x $\Delta\eta$.

The BEMC is a sampling calorimeter and the core of each calorimeter module comprises of a lead-scintilator stack and shower maximum detectors. It is made of 41 layers, where 21 layers are active scintillators that measure deposited energy of traversing charged particles and between them there are lead absorber plates. As a charged particle traverses these lead layers it produces an electromagnetic shower. This shower is detected by scintillators that convert energy of particle from the shower into the light and according to intensity of light we are able to determine amount of deposited energy of the charged particle. The actual deposited energy in the calorimeter depends on the type of particle and thus allows its identification.

The thickness of the BEMC detector is approximately 20 radiation lengths for an electron. The radiation length is defined as a distance that a high energy electron has to pass to lose $1/e$ of its original energy by radiation referred to as bremsstrahlung. Energy-momentum ratio E/p for high energy electron is 1. Due to this, it is expected that electrons and photons are completely stopped in the BEMC because they lose their whole kinetic energy. In contrast the cross section of hadrons with lead is much smaller in comparison to electrons. This means that hadrons are less ionizing particles $E/p < 1$. They do not lose their whole energy in the detector and they pass through it. Consequently, it is possible to distinguish high energy electrons form hadrons. By measuring deposited energy of high energy particles in the BEMC and by detecting their produced showers, we are able to study high p_T processes as leading hadrons and jets.

3.2.4 BEMC data

This section presents a sample of data which was collected by the Barrel Electromagnetic Calorimeter in Au+Au collisions in Run 11. These data were selected by the High Tower trigger. In my future diploma thesis, I will use this sample of data for jet analysis. Figure 3.6 depicts distribution of total energy with a cut of $E_{cut} >$ 2 GeV in $\eta - \phi$ plane. We can observe a some blank area around $\eta \in (0.2; 0.4)$ and $\phi \in (-0.6; -1.2)$ which corresponds to a dead region of the BEMC in Run 11. In addition some towers showed during data taking period abnormal behaviour manifesting itself in an unusually large energy deposition. This so called "hot towers" can be seen in Figure 3.7 which shows distribution of total deposited energy in each tower of the BEMC in Run 11. Prior to my future jet analysis, a detailed quality assurance of Run 11 BEMC data will be therefore needed.

3.2.5 Beam Beam Counter

There are two Beam Beam Counters (BBCs) on both sides of the STAR detector. They are located 3.5 m before the intersection point in STAR and surround the beam pipe. They cover pseudorapidity in the interval of $2.1 < |\eta| < 5.0$. The main function

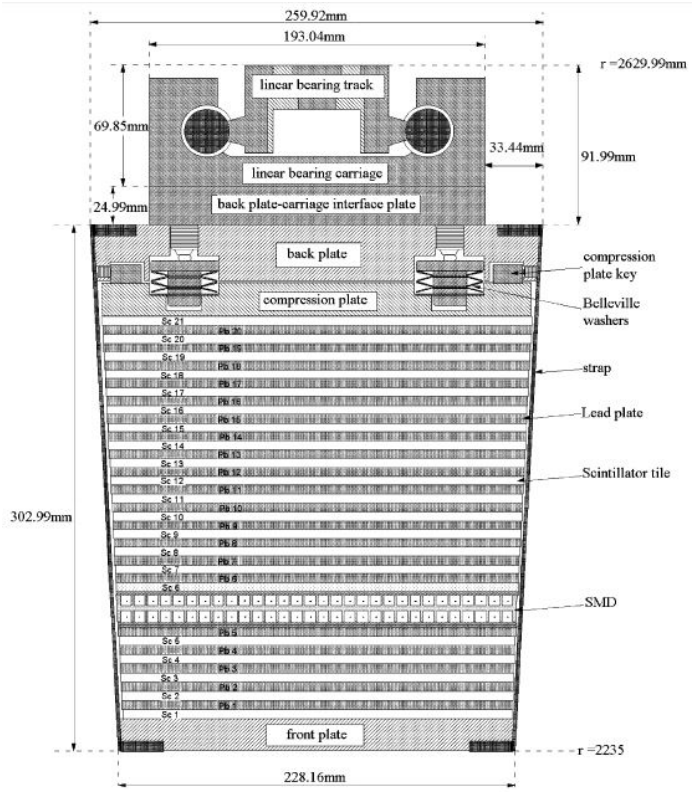

Figure 3.5: A schematic view of the BEMC module [30].

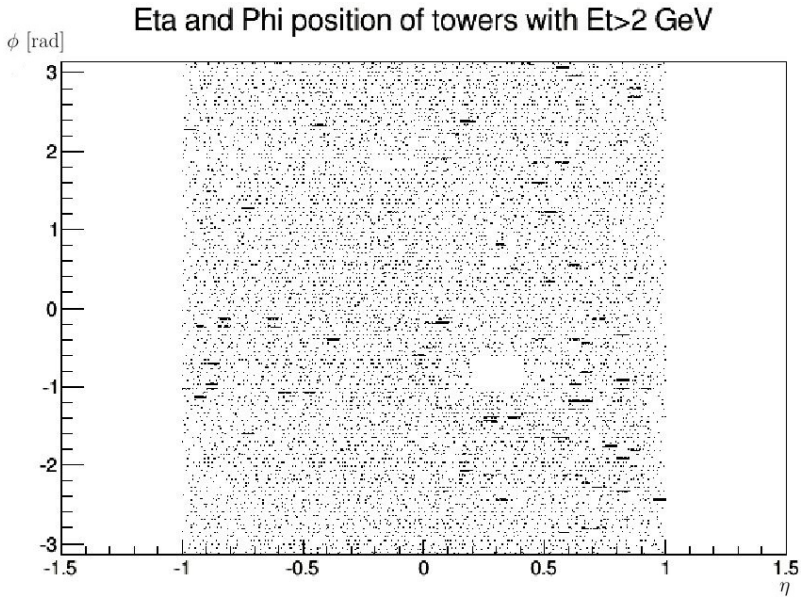

Figure 3.6: Distribution of total deposited energy in $\eta - \phi$ plane with cut $E_{cut} > 2$ GeV.

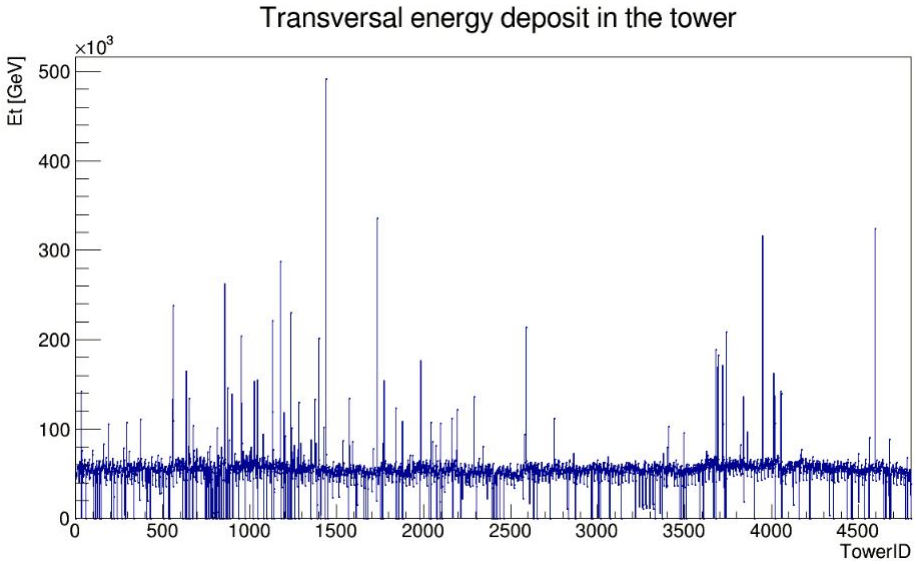

Figure 3.7: Total deposited energy in each BEMC tower in Au+Au collisions from Run 11 data.

of the BBC is to locate the position of a collisional vertex and determine collision centrality. The BBC consists of two rings of hexagonal scintilators.

3.2.6 Vertex Position Detector

The capability of the Vertex Position Detector (VPD) is determination of z position of the primary vertex - the point of collision. The VPD measures the start time for the TOF. It covers pseudorapidity $4.24 < |\eta| < 5.0$. There are two VPDs (West and East) located on both sides of STAR in the distance of 5 m from the intersection point and they surround the beam pipe. The VPD consists of 19 detectors, each of them composed of a lead converter followed by a fast plastic scintilator that is read out by a photomultiplier tube (PMT).

3.2.7 Muon Telescope Detector

The Muon Telescope Detector (MTD) [31] enables detection of muon pairs from QGP thermal radiation, quarkonia, light vector mesons and heavy flavor through semileptonic decays. These processes can be studied also through photons or electrons, but in comparison to muons they have larger background. The MTD is situated on the top of the solenoidal magnet. Its location is convenient because there is very low hadronic background. Muons are more penetrating than hadrons therefore mainly muons pass through the whole STAR and reach the MTD. Thus measurement of signal are with a low noise. For this reason we are able to distinguish and observe different Υ states. The MTD covers only 45 % of the full azimuth, its pseudorapidity coverage is $|\eta| < 0.5$ and its radius is 4 m. In the MTD there is installed a similar detection system and technology (MRPC) as in the TOF.

3.2.8 Heavy Flavor Tracker

The main function of a new Heavy Flavor Tracker (HFT) [32] is to precisely determine the secondary vertex of mesons that rapidly decay and contain heavy quarks, like D^0 or B^0. The HFT is a system of two detectors: a silicon pixel detector and an intermediate silicon tracker. The HFT improves analysis of heavy flavor and it is located in the center of STAR. The minimal radius of the HFT is only 2.5 cm and hence it tightly surrounds the beam pipe that had to be thiner than in another place at RHIC. The HFT is the first detector of STAR through which a particle passes.

3.2.9 Trigger system

In a typical Au+Au collision at $\sqrt{s_{NN}} = 200$ GeV, a large amount of data is produced, but technically it is not possible to analyze and register all data from all events, because the operating speed of STAR detectors is smaller than collision rate of RHIC. Therefore we need to reduce the rate of readout and for this function a trigger system is used.

The STAR trigger system is divided into four Levels: 0, 1, 2, 3 [33] . It uses information measured by fast detectors and based on knowledge of this decides whether a given event is suitable to trigger on and to be registered. The main fast detectors used for triggering are ZDC, VPD, BBC, TOF and BEMC. Level 0 consists of ZDC, VPD and BBC. Each collision is monitored by detectors of Level 0 that govern if the collision fulfills defined requirements or not. The capability of the ZDC is monitoring the luminosity and on the basis of detected number of spectators to determine centrality of the collision.

If the event is evaluated positively then the Level 1 and 2 starts. They are more time-consuming due to complex analysis of the trigger data. The main aim of Level 1 and 2 is to determine if the event fulfils more finely grained criteria. Simultaneously digitalization process and data transmission phase of the TPC take place and they can be aborted by these two Levels if data do not comply. Level 3 represents on-line analysis preformed by large CPU farms. Produced data are reduced and stored by a Data Acquisition System (DAQ) on tapes using technology of High Performance Storage System (HPSS).

Chapter 4

Jets

4.1 Definition of a jet

One possibility to study strong interaction and properties of QGP is observation and analysis of jets, which are experimental signatures of quarks and gluons. Jets are narrow conical sprays of particles, which are produced during the initial stage of ultra-relativistic proton or heavy ion collisions. In the early stage of the collision partons from incoming nuclei scatter and recede form each other. A large amount of energy is released in a very short time. This fact causes, that new pairs of quark-anti quarks are produced and they move along the trajectory of the original leading parton. The scattered parton has a large amount of kinetic energy and this energy is gradually lost by gluon radiation and also by production of quark-antiquark pairs, it is referred to as a fragmentation. To the fragmentation it is related the fragmentation function $F_i^h(x,t)$. It gives distribution of momentum fraction x for hadrons of type h in a jet initiated by a parton of type i, that is produced in a hard process at scale t [34]. New partons are colour charged and therefore they cannot remain free. They combine together and form colourless hadrons, that is why this process is called hadronization. It implies that the jet is a collimated shower of particles, mainly hadrons (mostly protons and pions) and posses same kinematic properties as a parton, from which it was created. Thus by observation and analysis of jets we can obtain useful information about collision or medium created in the collision area.

Jets are always produced in pairs of opposite direction ($\Delta\phi \approx \pi$) in their centre of mass reference frame, because an emerging quark and antiquark or particles that are produced during hadronisation process have to conserve momentum. Such events are called di-jet events. They are the most common in p-p collisions. But also sometimes a quark radiates a gluon before hadronisation. The gluon fragments producing a new jet. Therefore we can also observe three-jet, four-jet... events.

According to the parton type, from which a jet originates, we divide jets into several categories. For example a jet originated from a heavy flavor quark b, t, c or jets created from light quarks. In the collision a short living particles are produced. But we are not able to observe them directly, because they decay before reaching a detector. They can be however identified based on our knowledge of their decay channels. The point where a measured particle was created is called a primary

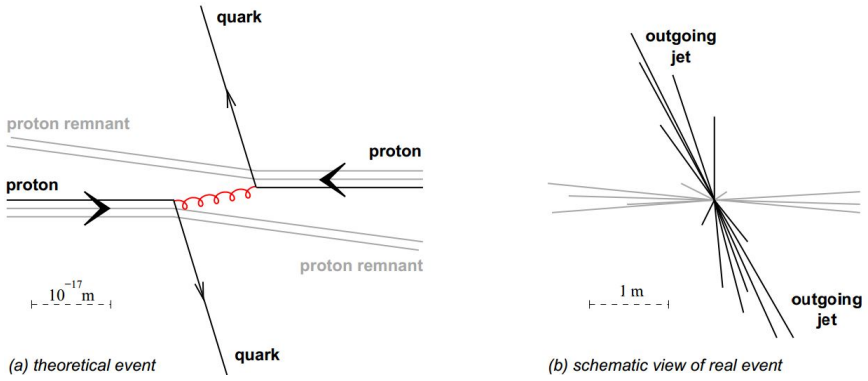

Figure 4.1: (a) Theoretical interpretation of p+p collision, (b)schematic representation of real event [35].

vertex. Then after a while the particle decays and the point where products of its decay arise are assigned to a secondary vertex.

In order to explore the QGP by jets, it is necessary to have techniques that enable jet studies. Examples of the most used techniques for jet analysis are:

- jet reconstruction by jet algorithms (described in more details in chapter 5)
- jet hadron correlations - they work already with reconstructed jets (explained in chapter 6)
- flavor tagging (b-tagging) - searching for jets created from heavy flavor quarks e.g. b quark [36]

4.2 Jet levels

From the formation to the observation of hadrons that are produced by scattering of two partons of colliding nuclei, a jet undergoes a complicated process. Jet evolution can be divided into three levels [37] and they can be seen in Figure 4.2:

- Parton level - the jet is formed by a cluster of partons. This level is calculated by perturbative Quantum Chromodynamics and it uses two approaches: Leading Order (LO) and Next to Leading order (NLO).
- Particle level - the jet is formed by hadrons in the final state. This level is used for generation data in Monte Carlo simulations.
- Calorimeter or Detector level - represents all energy towers or signals that are registered by detectors in $\eta - \phi$ plane. To each signal is assigned information about tracks, energy or momentum and these data are used for jet reconstruction.

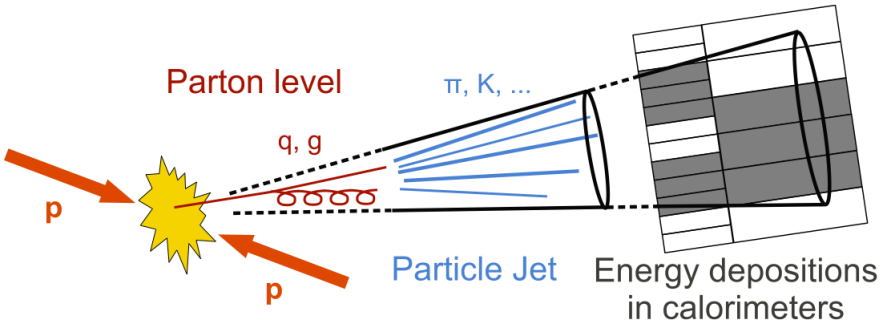

Figure 4.2: Evolution of a jet [38].

4.3 Jet background

During and immediately after the collision a large amount of particles is produced and detected. In this high multiplicity environment particles within jets are also among them. But we are interested in jets that originate from the initial stages of the collision, when the fireball is created and hard scattering occurs. In the large amount of signal in a detector it is necessary to find particles that belong to the initial partons. Jets are affected by background consisting of particles with low p_T originating from several sources [39]:

- Underlying event - products of interactions between hadron remnants that are produced in heavy-ion collisions. Underlying event also includes multiparton interactions and initial and final state radiations
- Pileup - multiple nucleon-nucleon interactions created by crossing bunches of particles in an event

These low p_T particles are roughly uniformly distributed among measured data. The majority of them do not belong to a jet, but during jet analysis they might end up in a jet and modify it [40]. But we do not know exactly which particle belongs to jet or not, because jet has no unique definition. Thus there are jet algorithms that are used for jet reconstruction and techniques for background subtraction that are described in the next chapter.

Chapter 5

Jet algorithms

5.1 Definition

Jet-finding algorithms are used for jet reconstruction. They are widely used in data analysis from experiments at the LHC or RHIC. But they were also applied on data from experiments that are not already in operation, for example Fermilab, LEP... Jet algorithm is a set of procedures and instructions that aim for identifying jets as the observable counterparts of the perturbative concept of partons. Their right definition is crucial for comparison of experimental analysis to theory. The jet-finder is applied both to perturbatively predicted partonic configurations and to observed hadronic configurations and one then directly compares distributions for the predicted partonic jets and the observed hadronic jets. Though partonic and hadronic jets are not equivalent, there is strong evidence that the comparison can be performed with controlled accuracy [41].

The main goal of jet algorithms is to cluster a set of charged tracks and neutral towers measured by detectors into jets in $\eta-\phi$ plane. At the beginning, the algorithm selects a set of particles, which are typically emitted close to each other in space. At experimental level these particles are hadrons or calorimeter towers and partons in a pQCD calculation level. During the jet analysis, each jet is assigned a four-momentum $p = (E, \vec{p}) = \sum(E^i, p_x^i, p_y^i, p_z^i)$ and transverse momentum p_T as was defined in the first chapter. The jet algorithm combines momenta of measured particles to form the momentum of a jet. The momentum addition rule is called the recombination scheme. Reconstructed jets have the same kinematic properties as the original partons, which were produced in the hard scattering process. This allows us to study them or at least indirectly observe their properties.

5.2 Attributes of ideal jet algorithm

An ideal jet algorithm has to fulfil several theoretical and experimental attributes, because there is no exact solution or definition of a jet. The result of a jet usually depends on a type of algorithm used. To get a correct result or at least a result, which converges to the right solution and complies with the demands of the study, every reliable jet algorithm has to fulfil criteria following [37]:

- Fully specified: jet selection process, the jet kinematic variables, the various

corrections, specifications for clustering, energy and angle definition, and all details of jet splitting and merging should be clearly and completely defined.

- Detector independence: application of jet algorithm should provide similar results on various types of detectors, which differ from each other in size, cell type, detector segmentation, energy response or resolution.

- Order independence: algorithm behaves equally at the parton, particle and detector level.

- Infrared safety: algorithm should find a solution which is insensitive to any soft radiation in the event - any radiated soft gluons or products of hadronization will not influence existence, number or shape of a jet. On the detector level of a jet, algorithm searches around towers with some minimum energy. Tower is a minimal resolution point of a detector. On the parton level, the perturbative calculations are without any infrared singularities. Figure 5.1 illustrates infrared safety of a jet algorithm.

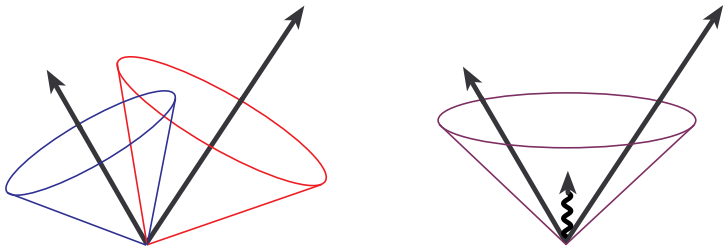

Figure 5.1: Infrared safety of a jet algorithm [37].

- Collinear safety: On the detector level, when two particles move very close to each other, their mutual distance does not influence and change the final jet or final number of measured jets. Let us assume two particles moving together, which mutual distance is short and have smaller energy than other particles in arising jet. They can be detected together in one tower of the detector. In this case detector considers them as one signal and the final jet could be reconstructed incorrectly or not at all. If the jet algorithm is not influenced by this effect, this characteristic is denoted collinear safety. On the parton level, the perturbative calculations are without any collinear singularities. Figure 5.2 illustrates two cases of collinear safety of a jet algorithm.

- Maximal reconstruction efficiency - all relevant jets are reconstructed

- Easy use - jet algorithm is able to analyse and work with typical experimental data.

- Efficient use of computer resources: Because of the enormous number of analysed data measured by detectors, especially in heavy ion collisions, where in comparison to p+p collisions there is several times larger amount of data, the jet algorithm should provide jet identification with a reasonable computing

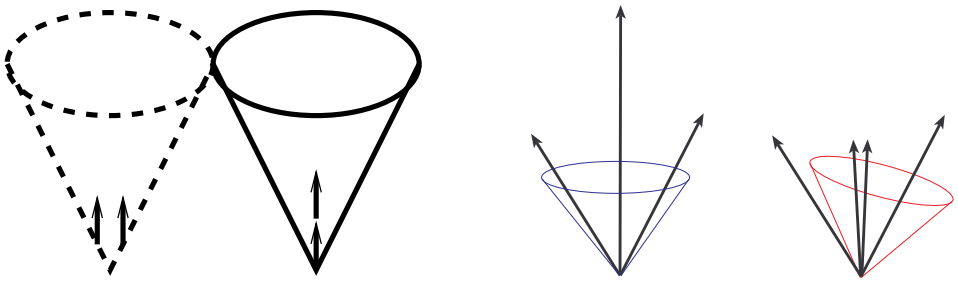

Figure 5.2: Collinear safety of a jet alorithm [37]

time. For description of the computing time, a time complexity of an algorithm $O(f(N))$ is defined and this function represents evolution of time of computation, where $f(N)$ is a specific function for the algorithm, N is a number of particles in an event. The computation time significantly depends on N and we will compare speed of various algorithms at the end of section 5.3.

5.3 Classes of jet algorithms

During the years of the jet study there has been a demand to the jet algorithms, which can reconstruct jets fast with the high precision and implement attributes mentioned above. Many types of jet algorithms were developed, which differ slightly form each other in some attributes and in their scheme of jet finding, These attributes are: sequence of steps to find a jet, initial energy and momentum parameters, collinear and infrared safety, boundary sensitivity and sensitivity to non-perturbative effects, e.g. hadronisation and underlying event contamination. According to the selection of starting particle, jet algorithms can be classified to seedless and seeded that start by choosing the most energetic particle in the event, which is called a seed. The seedless jet algorithm looks for all stable solutions of jet from all detector entries without choice of any seed. Moreover, jet algorithms can be divided into two groups: cone and sequential recombination.

5.3.1 Cone Algorithms

Seed cone Algorithm

The cone algorithm forms or approximates jets of particles into a cones around a direction of dominant energy flow. The vertex of the cone is in the location of decay of parent particle. The main goal of this algorithm is to look for a stable cone of jet in various iteration steps and then process splitting and merging. The cone algorithm starts by drawing a circle of a specific radius $R = \sqrt{\Delta\eta^2 + \Delta\phi^2}$ (where R is a radius of a cone) in $\eta \times \phi$ plane around the highest p_T or the most energetic particle of the collision, which is called seed (On the detector level seed is the tower with the highest energy). Then the total transverse momentum and energy is computed including contributions from all particles located inside the cone. This leads to formation of a new point in $\eta \times \phi$ plane which is subsequently used as the center of a new trial cone. This iteration process runs until the stable cone is found and everything inside the cone is proclaimed as a jet. But it is important to mention, what means that the

cone is stable. A jet is proclaimed as a stable one if direction of a resulting stable jet (sum of momentum vectors of all particles inside a jet) is identical with the axis of a starting particle. But if the difference between axis of resulting jet and starting particle is larger than determined criterion then it is necessary to recalculate the momentum of a trial cone founded. A new cone is created with the same radius R and compared to the the axis of previous cone again.

After iteration process of stabilization of jets, a procedure of splitting or merging is needed to be run, because areas of jets can overlap. Two jets will be merged if the percentage of shared transverse energy of the lower p_T jet is greater than 50%, otherwise they are split [37]. During clustering process not all particles form the list are contained within jets, some of them comprise lost signals. Because of an enormous amount of particles in the list of the event, on the beginning of computation, it is defined a minimum energy in a tower, so particles, which energy is below this threshold are not taken into consideration. The cone algorithm behaves as a collinear, but its disadvantage is infrared unsafe. But on the other hand it is very fast and simple O(N).

SISCone algorithm

Seedless infrared safe algorithm (SISCone) is the next cone algorithm, but in comparison to cone, SISCone is infrared and collinear safe. The main aim of this algorithm is also to identify all circular enclosures - cones and test their stability. Its basic steps are described and depicted in Figure 5.3 as follows [42]:

1. A circle of radius R around a point, which represents a particle is put into an event in $\eta \times \phi$ plane.

2. The circle is moved in a random direction and until the edge of the circle hits a point outside.

3. The circle is rotated around the boundary point until another one touches the edge of the circle.

4. The procedure above is repeated until all points in nearby area of starting points are included.

5. All particles defined by pairs of edge points form a jet.

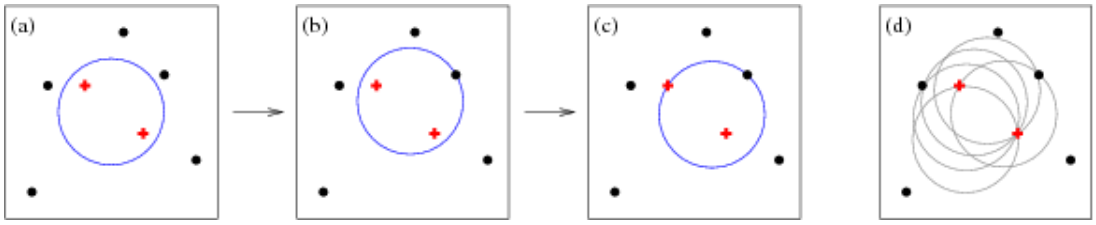

Figure 5.3: Scheme of the SISCone algorithm [42].

5.3.2 Clustering algorithms

The next category of algorithms are jet clustering algorithms (or alternatively jet sequential recombination algorithms). These algorithms have become in the last years the main tool for analysing data from high energy pp collisions. In comparison to the cone algorithms, sequential recombination algorithms are based on specific selection of a starting particle and then sequentially add other particles that are close enough to the arising jet. Their advantage is that they collect the most of the particles that are radiated from an original parton so the efficiency of reconstruction is high [41]. But their disadvantage is slowness in high multiplicity environment.

This class of jet algorithms starts with a list of preclusters and empty list of jets. Preclusters are signals or hits measured by a detector and they are formed from particles, partons or calorimeter cells. Initially a vector $(E, \vec{p} = E(1, \cos\phi \sin\theta, \sin\phi \sin\theta, \cos\theta))$ is assigned to each precluster, where E is the energy of the precluster, ϕ is the azimuthal angle and θ is the polar angle with respect to the beam axis. Then the square of transverse momentum p_T^2 is calculated for each precluster
In order to find final jets from preclusters, algorithm carries out several steps outlined bellow [37]:

1. The clustering algorithm begins with a definition of distances d_i and d_{ij}:

   - For each precluster i in the list, define distance from the beam

   $$d_i = p_{T,i}^{2n} \tag{5.1}$$

   For each pair (i, j) of preclustes $(i \neq j)$, define distance between i and j

   $$d_{ij} = min(p_{T,i}^{2n}, p_{T,j}^{2n}) \frac{\Delta_{ij}^2}{D^2} \tag{5.2}$$

   where $\Delta^2 = (y_i - y_j)^2 + (\phi_i - \phi_j)^2$ and p_{Ti}, y_i, ϕ_i are respectively the transverse momentum, rapidity and azimuth of precluster i. For each particle or tower the transverse momentum is defined as:

   $$p_{Ti} = \frac{E_i}{c} \sin\theta_i \tag{5.3}$$

   where θ_i is an angle between the direction of a particle and the beam of colliding nucleons. R is a radius parameter that represents size of a jet and the minimum distance between two pairs of jets i, j. Simply, R is a minimal radius of a jet and typical value used in data analysis is 0.2 to 1.0. Parameter n governs the relative power of the transverse momentum (or rather energy) versus geometrical (Δ_{ij}) scales. Different values of $n \in -1, 0, 1$ correspond to three clustering algorithms: k_T, $anti - k_T$ and Cambridge/Aachen, which will be discussed later.

2. After computation of all distances d_i, d_{ij} and excluding values below a jet resolution threshold d_{cut}, the minimum of them is found and labeled as d_{min}.

3. The next step of algorithm depends on attribute of d_{min}:

- If d_{min} is a d_{ij}, preclusters i and j are removed from the list and replaced by a new merged precluster: $p_{ij} = p_i + p_j$ and $E_{ij} = E_i + E_j$
- If d_{min} is a d_i, the corresponding precluster can not be merged and it is removed form the list of preclusters and add it to the list of jets.

4. If any preclusters remain, values d_{min} are calculated again and the whole process of jet finding is repeated. It can happen that a jet overlaps with another one, then the common area is assigned to a jet with higher or lower transverse momentum according to the algorithm used.

In general, all jet clustering algorithms are infrared and collinear safe.
As was said before, there are three most commonly used clustering algorithms: k_T, anti-k_T and Cambridge-Aachen. They differ from each other in calculation of distance between particles. The main characteristics of clustering algorithms are as follows:

k_T algorithm
From Eq (5.2), where the power of energy is positive, it is obvious that k_T algorithm recombines first particles with low p_T close to each other in space. It implies its sensitivity to soft background because it prefers soft particles. Use of the k_T algorithm in heavy-ion collisions might cause problems because if we compare jet reconstruction in a hard event without background to an event with added soft particles, resulting jets will be different. Not only the energy of jets is higher due to energy of soft background, but also jet shapes are changed and less regular. This feature is called back reaction. Therefore the k_T algorithm is usually used for estimation of background. Scheme of k_T algorithm is depicted in Figure 5.4.

$anti - k_t$ algorithm
The anti-k_T inclusive jet finding algorithm belongs to a class of jet clustering algorithms, where the power of the energy scale is negative. It acts as an idealized cone algorithm [43], because reconstructed jet shapes are regular and quite circular. Unlike the k_T algorithm, the anti-k_T algorithm is resilient to the soft background, because it clusters first particles with the highest p_T. Soft particles are connected to hard one before recombination among themselves. This leads to the high suppression of the effect of the back reaction.

Cambridge/Aachen algorithm
The power of energy is 0 in this algorithm. It means that momentum of particles is not taken into consideration at all, therefore recombination is based only on spatial separation.

It is also important to mention, that each algorithm has specific computing time. Comparison of speed, infrared and collinear safety of jet algorithms is given in Table 5.1. We can see that the fastest algorithm is the Cone, but in comparison to other algorithms its disadvantage is infrared and collinear unsafety. SISCone and clustering algorithms are slower, but they are effective and reliable in data analysis. Computation time of jet algorithms is compared in Figure 5.5.

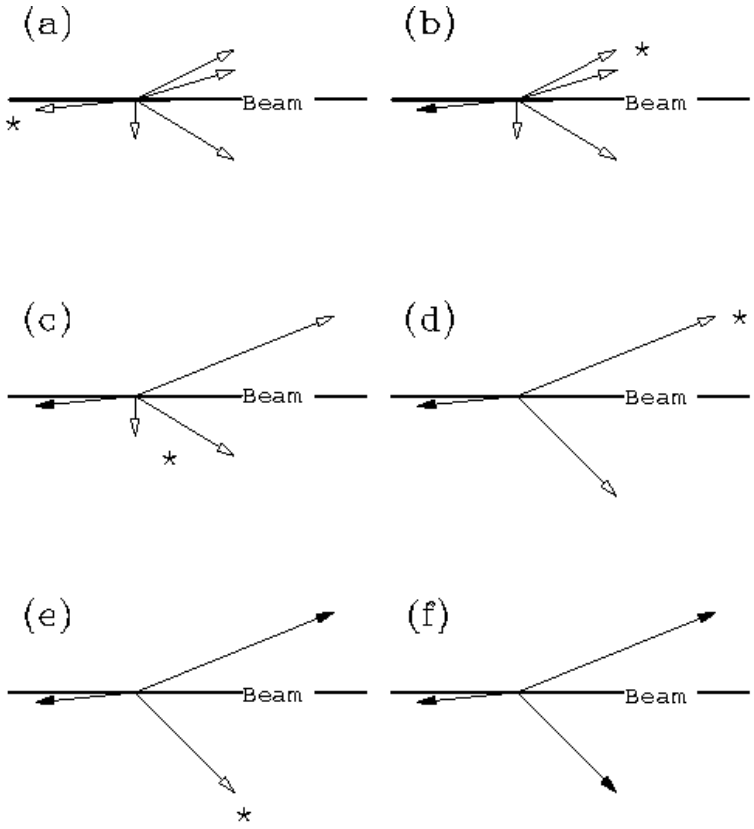

Figure 5.4: Scheme of k_T algorithm [37]

Algorithm	Speed	Infrared safety	Collinear safety
Cone	N	no	no
SISCone	$N^{3/2}$	yes	yes
k_T	$N \ln N$	yes	yes
anti-k_T	$N \ln N$	yes	yes
Cambridge-Aachen	$N \ln N$	yes	yes

Table 5.1: Comparison of speed, infrared and collinear safety of jet algorithms [40].

5.4 Jet areas

Jet area is a measure of susceptibility of a jet to soft radiation (underlying event, pileup), that is uniformly distributed in rapidity and azimuth around the jet. Jet areas are used for subtraction of the jet contamination by soft radiation. There are two main definitions of jet area: passive and active [44]:

- **Passive area**: it is a measure of the susceptibility of the jet to pointlike radiation. A single ghost particle is added to the event. Then the region in which a jet clusters with a single ghost is defined as a passive area. The passive area geometrically equals to πR^2.

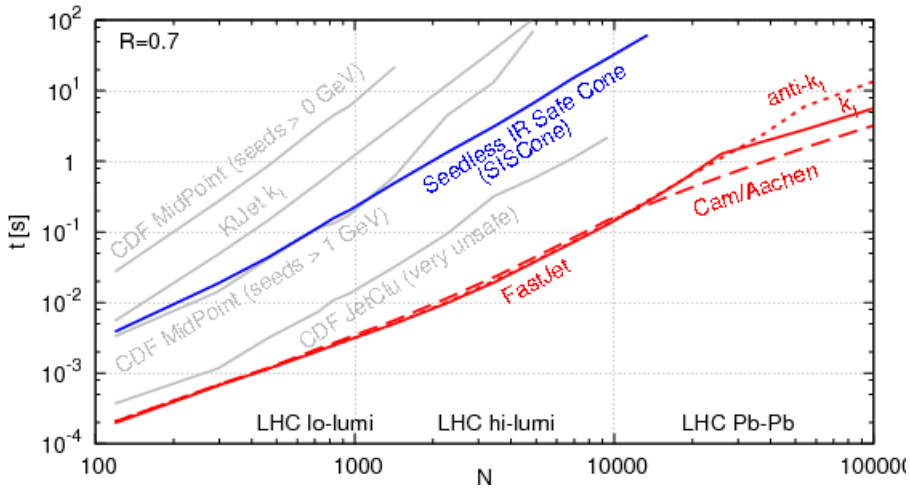

Figure 5.5: Timings for the clustering of a simulated 50 GeV di-jet event with Pythia) [40].

- **Active area**: a dense coverage of soft ghosts g_i each with an infinitesimal p_T, randomly distributed in rapidity and azimuth with density distribution per unit area ν_g is added to the event. Ghosts might cluster with each other and also with hard particles. Because of infrared insensitivity of jet algorithm, the addition of ghosts does not influence the shape or the momenta of the final jet. The number of ghosts in a jet is used as a measure of jet area. In comparison to the passive area, which has shape of a circle, the structure of the active area is more complicated. In Figure 5.6 different area structures of various jet algorithms can be seen.

5.5 Background subtraction

A critical issue of each jet analysis is the background, mainly in heavy-ion collisions. Therefore it is important to exclude it by subtraction of background. The process when a background is subtracted from measured jets is called decontamination of a jet and it is carried out after all jets are found. The transverse momentum density of background ρ is estimated by using concept of jet areas [45] as follows [15]:

$$\rho = \text{median}\left(\frac{p_{T,i}}{A_i}\right) \tag{5.4}$$

where i runs over all reconstructed jets with transverse momentum $p_{T,i}$ and area of jet A_i in the event. In this case the seeded cone or k_T algorithm is used for jet finding. Then an event-by-event correction is provided for each jet with p_T:

$$p_{T,corr} = p_{T,raw} - A\rho \tag{5.5}$$

Jet reconstruction by traditional jet algorithms in the large soft background can produce besides real jets also fake jets. Thus jet production in the large background

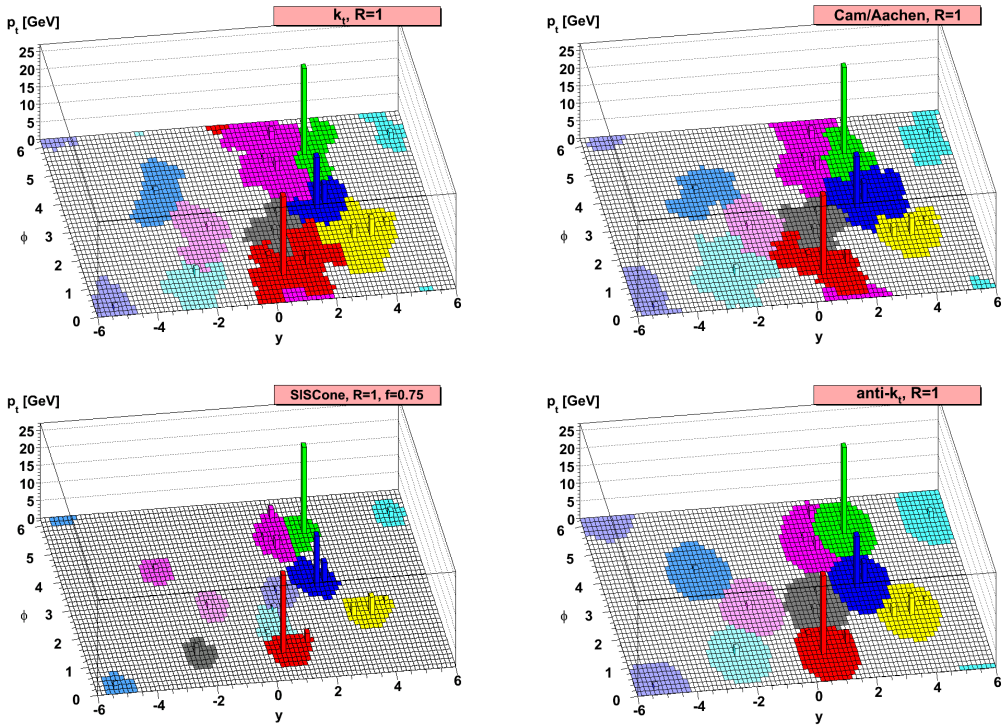

Figure 5.6: Comparison of areas of jet algorithms [43]

is above the intrinsic production of jets. Background with the fake jets impedes the detection of the low cross section signals. To restrain this problem, it was developed the Gaussian filter which was used in the jet analysis at the PHENIX experiment [46]. The Gaussian filter provides a jet definition more robust than traditional jet algorithms. The cone algorithm that has fixed geometry exhibits more stable behaviour in fluctuating background than dynamic shape algorithm (sequential recombination algorithm) e.g. k_T. The most of the jet energy is located near the centre of the jet and only small part of energy is in the periphery of the jet. For that reason it is necessary to have an algorithm that finds a maxima in the distribution of transverse energies using a weighting function (Gaussian filter) that is strongly peaked. Thus, a radially weighted cone jet algorithm is more suitable for heavy-ion environment, because has potential to find jet in the presence of fluctuating background. Jets reconstructed by Gaussian filter are found by locating the local maxima of the filter output (in the linear-circular convolution).

5.6 FastJet

The FastJet package [47] is a powerful software package used for jet analysis . It has been written in C++ by Matteo Cacciari, Gavin Salam and Gregory Soyez and includes a broad range of jet analysis tools. Fastjet provides fast implementations of all most used jet sequential recombination algorithms such as k_T, anti-k_T and Cambridge/Aachen jet finders. It can be extended by SISCone and other cone algorithms via plugin. FastJet also includes tools for calculating jet areas, performing background estimation of pileup and underlying events, background subtraction and for jet substructure analyses [47].

Chapter 6

Jet analysis at RHIC

Jets are well described in proton-proton collisions by perturbative quantum chromodynamics at parton level, therefore we are able to make calculations and theoretical predictions and compare them with experimental data. Full jet reconstruction in environment of heavy ions is more challenging than the p+p collisions due to large and fluctuating underlying soft background.

Jets can be created anywhere in the volume of the medium. If a pair of jets is produced on the edge of the medium, one of them that is closest to the edge can leave collision region without almost any change. The jet in opposite direction has to pass through whole volume of medium and therefore a significant modification of jet is expected. If we would study azimuthal distribution of hadrons with high p_T we will find out that jet traversing the medium loses energy because it is detected with a noticeable lower p_T in comparison to the first jet. The jet passing through medium is quenched. Due to the law of momentum and energy conservation the missing energy of the quenched jet manifests itself in two effects, referred to as a softening or broadening. Softening means that p_T of hadrons in the quenched jet is shifted to lower values and broadening is scattering of energy into a larger angle. The presence of jet quenching is therefore demonstrated by suppression of the high-p_T hadron spectrum and modification of energy-particle flow of final jets, which is represented by softer hadron spectra, larger multiplicity and increased angular broadening [21]. Comparison of quenched and un-quenched jet and study of modification of the quenched jet provide important information about properties of the medium and its formation at earliest stages of the collision.

For investigating of nature of jet quenching, several observables with different sensitivity can be used and they are discussed in detail below.

6.1 Di-hadron and jet-hadron correlations

Di-hadron correlations are used for studying jet medium modification on a statistical basis. At the beginning we select a hadron with high p_T with an azimuthal angle ϕ_{trigg}. This high p_T particle is referred to as a trigger. Trigger is paired with all other particles in the event known as associated particles, especially it is associated with another particle with lower p_T than trigger [48]. Then it is necessary to define area around trigger with angle ϕ_{trigg}, it is denoted near-side and the opposite

side around angle $\Delta\phi \approx \pi$ is denoted away side.

In p+p collisions, the distribution of associated particles shows a peak on the near side at $\Delta\phi = 0$ and on the away side at $\Delta\phi = \pi$, where $\Delta\phi$ is the azimuthal angle between the trigger and associated particles. The near-side and away-side scheme is depicted in Figure 6.1. The near-side particles (left), which are the leading hadron (trigger) and subleading hadrons form a near side peak at angle of $\Delta\phi = 0$. The away-side peak results from the opposing hadrons created in the hard scattering. In heavy ion collisions the away-side peak is suppressed because particles have to propagate almost the whole volume of medium.

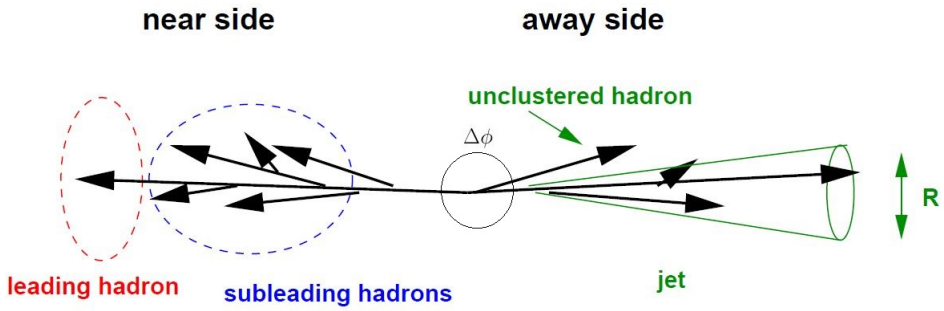

Figure 6.1: A sketch of various ways of observing a hard back-to-back event experimentally [49].

In di-hadron azimuthal correlations we are interested in angular distribution of the associated particles with respect to the trigger particle. The correlation function is used to deduce information about high p_T particle interactions with the medium during propagation. An example of di-hadron correlation function for minimum bias and central d+Au collisions (a) and for p+p and central Au+Au collisions (b) at $\sqrt{s_{NN}} = 200$ GeV is depicted in Figure 6.2. Trigger particles are selected with a cut of $4 < p_{T,trigger} < 6$ GeV/c and cut for associated particles is $2 < p_T < p_{T,trigger}$. In Figure 6.2 we can observe near-side peak ($\Delta\phi \approx 0$) that is similar in all three systems: p+p, d+Au and central Au+Au collisions. In d+Au, no large suppression of away-side peak is observed, thus no hot and dense medium is created. But lower part (b) of the figure shows a significant suppression of away-side peak in Au+Au relative to p+p and d+Au. The suppression phenomena in Au+Au is due to final-state interactions with dense system created in the collision.

There are also pseudorapidity correlations, in which we are interested in pseudorapidity distribution of the associated particles with respect to the trigger particle. A few years ago, a long range pseudorapidity correlation at near side referred to as a ridge has been unexpectedly observed in Au+Au collisions by STAR [50]. The ridge can be seen in Figure 6.3. Later it was also observed in Pb+Pb collisions at the LHC, but more surprisingly also in small collision systems such as p+p, p+Pb and d+Au. The origin of the ridge is still a challenging question, but the currently preferred scenario is that it originates from fluctuations in the initial state [51].

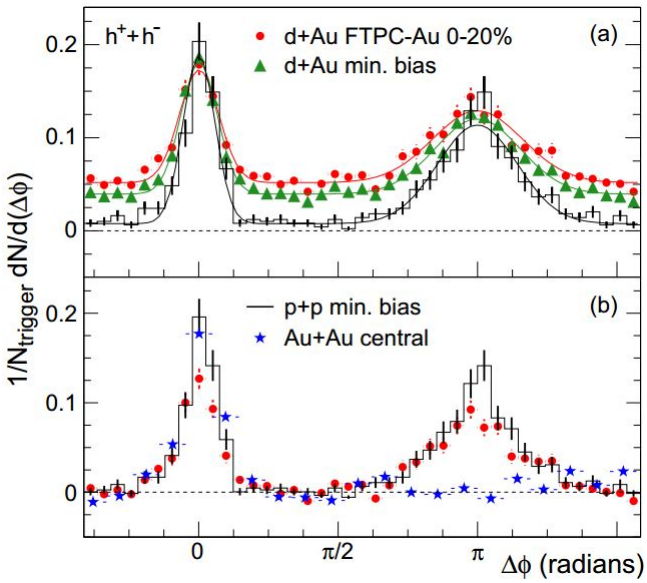

Figure 6.2: (a) Two-particle azimuthal distribution for minimum bias and central d+Au collisions and for p+p collisions. (b) Comparison of two-particle azimuthal distributions for central d+Au collisions to those seen in p+p and central Au+Au collisions [17].

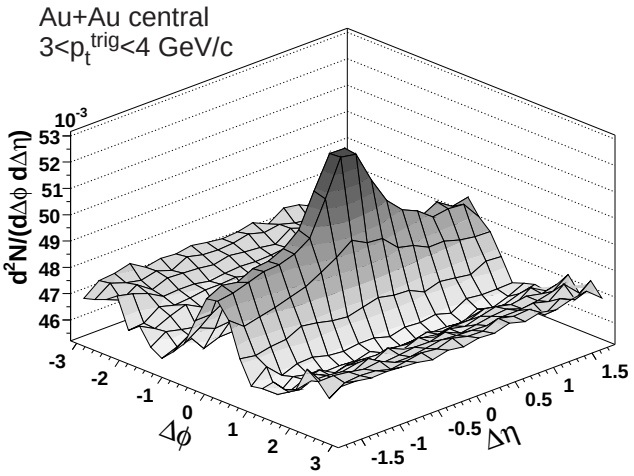

Figure 6.3: A schematic diagram demonstrating the structure of the near-side jet with the ridge [50].

Instead of di-hadron correlations, now jet-hadron correlations are used more, because jet reconstruction enables more direct access to the original energy of parton. In jet-hadron correlation, a trigger jet is selected and production of hadrons with lower p_T according to angle $\Delta\phi = \phi - \phi_{trigg}$ is studied.

An example of the jet-hadron distribution relative to the jet axis is shown on

Figure 6.4. This figure presents jet-hadron correlation for p+p and Au+Au collisions at $\sqrt{s_{NN}}$ = 200 GeV after background subtractions. Cut for trigger jet is $10 < p_T^{jet,rec} < 15$ GeV/c and cut for associated particles of two ranges are (a) $0.5 < p_T^{assoc} < 1$ GeV/c and (b) $4 < p_T^{assoc} < 6$ GeV/c. In plot (b) we can observe a significant medium-induced suppression of away-side associated hadrons in Au+Au with respect to p+p collisions. It can be also observed that the away-side peak in plot (a) is larger for Au+Au than for p+p collisions, because missing energy from suppressed high p_T away-side hadrons in Au+Au appears as an yield enhancement and broadening of the soft hadrons.

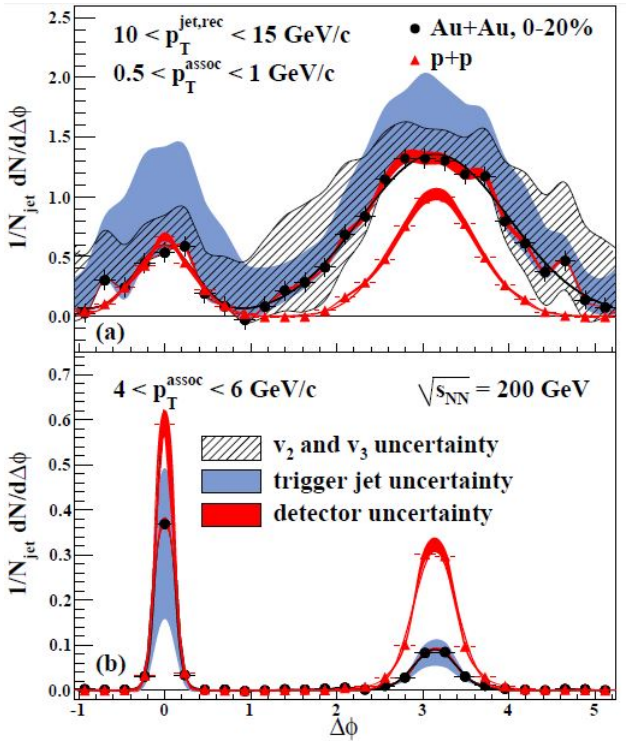

Figure 6.4: Jet-hadron correlations after background subtraction in Au+Au and p+p collisions [18].

6.2 Jet R_{AA}, fragmentation and cross section measurement

This section summarizes some results and examples of jet analysis at RHIC provided in recent years. Following text presents measurements of jet cross section, jet structure, jet fragmentation and correlation of fully reconstructed jets in $\sqrt{s_{NN}}$ = 200 GeV p+p and Au+Au collisions at RHIC. These measurements pf reconstructed jets provide insight into jet quenching in QGP. Results presented below are taken from articles [52] and [53].

The analysis described below reports inclusive differential jet production cross section, jet R_{AA} and ratios of cross sections. In this case inclusive jet production in p+p and in 10% the most central Au+Au events at $\sqrt{s_{NN}} = 200$ GeV were studied. Jets were reconstructed by two jet algorithms: k_T and anti-k_T with the resolution parameters $R = 0.2$ and R=0.4. Background is subtracted by the method described in the previous chapter.

The Figure 6.5 shows the differential cross section of inclusive jet production in p+p (left panel) and Au+Au (right panel) for k_T and anti-k_T algorithm.

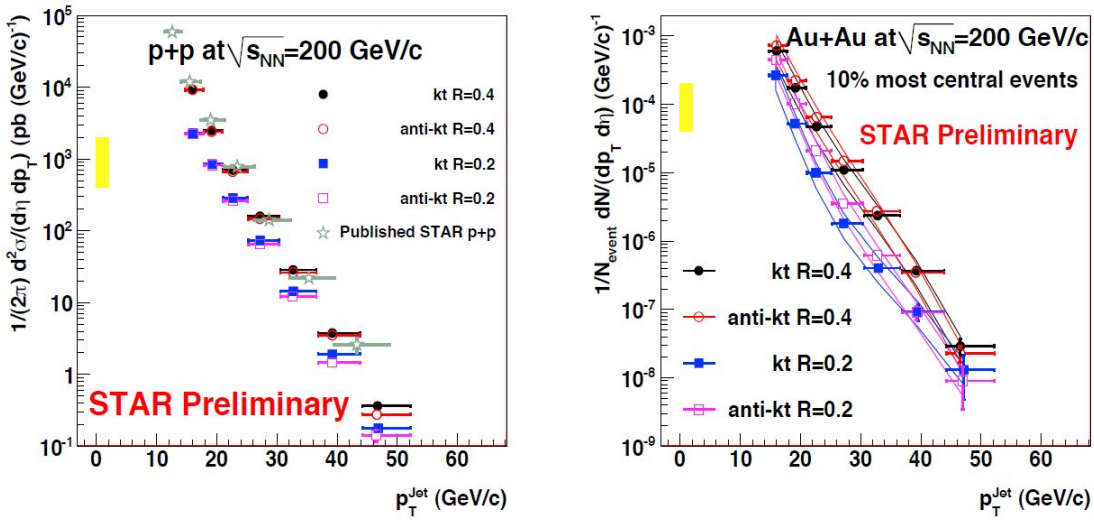

Figure 6.5: Cross section for inclusive jet production in p+p (left) and Au+Au (right) collisions [52].

The next Figure 6.6 presents nuclear modification factor R_{AA}^{jet}, the ratio of the jet yield in Au+Au and jet yield in p+p scaled by binary collisions. Within the large uncertainties, R_{AA} is compatible with unity. It can be seen that R_{AA} for $R = 0.4$ is significantly larger than R_{AA} for $R = 0.2$. But it is also possible to observe differences between k_T and anti-k_T algorithms. This difference is caused by different response of both algorithms to the heavy-ion background. The left panel shows the jet-yield ratio R=0.2/R=0.4, individually for p+p and Au+Au collisions. The ratio for p+p increases with p_T^{jet} and it is consistent with a Pythia simulations, but there are some differences with NLO calculation. Both plots also presents strong suppression for central Au+Au collisions in comparison to p+p. This fact indicates jet broadening in heavy-ion collisions.

Data for next analysis were collected by the TPC for charged particles and the BEMC at STAR for the neutral energy. The analysis is based on p+p collisions and 0-20% most central Au+Au collisions. Data were selected by an on-line High-Tower trigger in the BEMC with transverse energy $E_T = 5.4$ GeV and analysed by anti-k_T algorithm from the FastJet package. This di-jet analysis was performed on events with trigger jet and recoil jet. The problem of each analysis is background which was estimated and subtracted by the method described in the previous chapter. Background in central Au+Au events exhibits significant fluctuations, which were

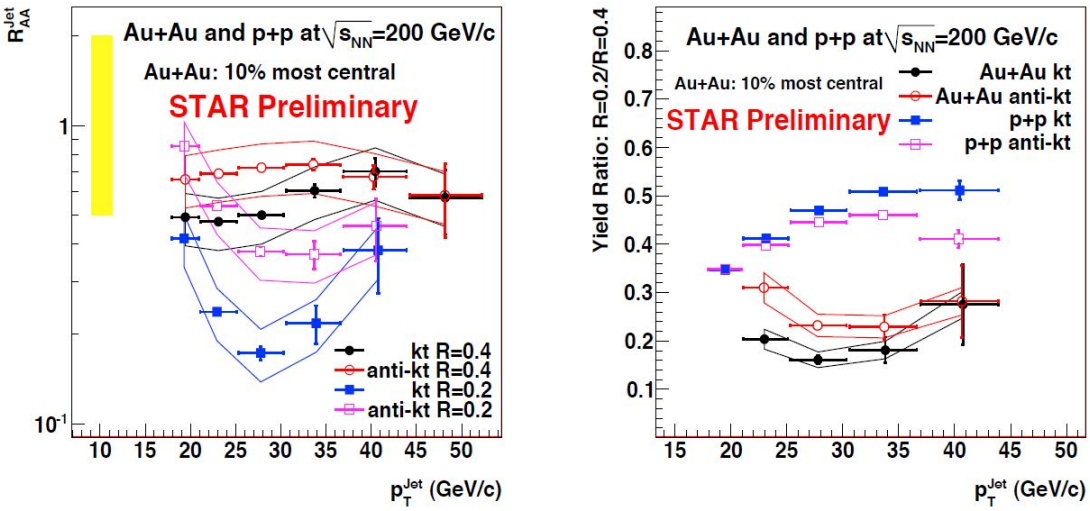

Figure 6.6: Ratios of inclusive jet cross sections in p+p and Au+Au collisions. Left: jet R_{AA}. Right: ratio of cross sections $R = 0.2/R = 0.4$ [52].

parametrised by a Gaussian width and then subtracted. In general, it is possible to suppress fluctuations of the background by imposing p_T cuts on particles in the jet. In the analysis, the strong trigger bias was used therefore a particular class of di-jets was selected. The minimum transverse momentum of 2 GeV/c for jet constituents was applied to have the same energy scale in p+p and Au+Au. Recoil jets were reconstructed with a minimal momentum of 0.15 GeV/c for jet constituents. The contribution of "fake" jets and hard scattering uncorrelated to the di-jet was minimized by requirement of $p_{T,rec}^{jet}$=10 GeV/c.

This analysis focuses on measurement of spectra of recoil jets, their comparison between p+p and Au+Au collisions and measurements of jet fragmentation.

Figure 6.7 shows (left) the recoil jet spectra in p+p and Au+Au events that are normalized to the number of trigger jets and (right) ratio of di-jet spectra, when Au+Au collisions are compared to p+p. The right figure shows a strong suppression of recoil jets in Au+Au with respect to p+p at the same jet energy. This observation could be explained via jet broadening, in which energy of a jet is not fully recovered in jet radius $R = 0.4$ with respect to p+p collisions. A shift of energy spectrum of recoil jets to smaller values of energy would be expected.

Figure 6.8 presents jet fragmentation distribution for recoil jets (left) and the ratio of the z distribution of p+p and 20% most central Au+Au (right). z is defined as $z = p_{T,hadron}/p_{T,jet}$. Jet fragmentation was measured for charged hadrons in radius $R = 0.7$ around the jet axis, while jet were reconstructed in $R = 0.4$. Background was estimated on the basis of spectrum of charged particles located outside the area of two reconstructed jets with the highest energy in Au+Au. Plots in Figure 6.8 do not shows any significant modification of jet fragmentation for $z > 0.2$ in contrast to the expectation of a softening of the jet fragmentation in Au+Au. Expectation of the softening of the jet fragmentation accounts for the measured high p_T hadron suppression. It is possible to explain the absence of jet fragmentation modification via jet broadening, when jet energy is not fully recovered in R=0.4 and energy in

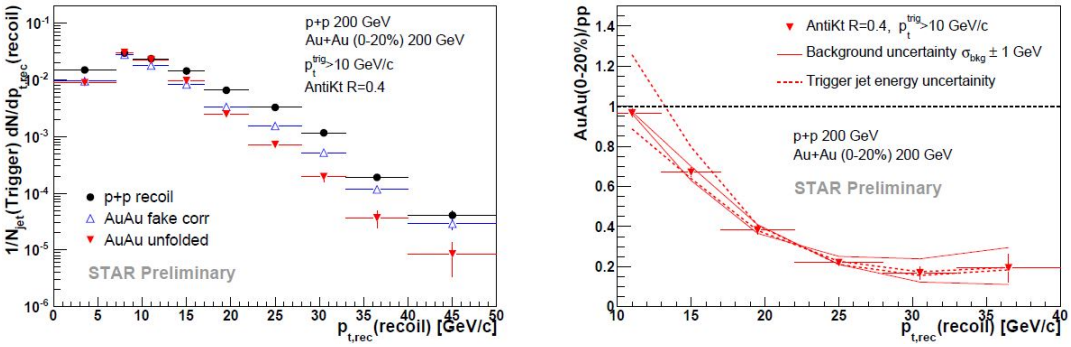

Figure 6.7: Left: p_T spectra of recoil jets in p+p and Au+Au. Right: ratio of p_T spectra of recoil jets in Au+Au to p+p [53].

this radius is underestimated. But in this case a shift in the spectrum of recoil jets towards lower energies would be expected and it would explain the result in Figure 6.7. To prove this scenario it is necessary to confirm if jet broadening happens beyond $R = 0.4$ or not.

The low z-part ($z < 0.1$) is still under investigation because it is dominated by the underlying background and can be therefore affected by uncertainness caused by background subtraction.

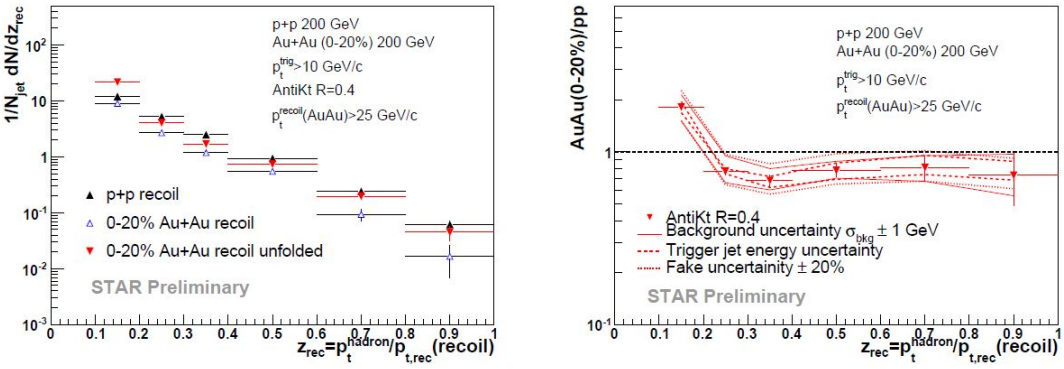

Figure 6.8: Left: Fragmentation function for recoil jets in p+p and Au+Au. Right: Ratio of the z distributions measured in central Au+Au event to p+p collisions [53].

6.3 Results from Hard Probes 2015

6.3.1 Semi-inclusive recoil jet spectra

This part of thesis presents most recent results from measurements of jet production at $\sqrt{s_{NN}} = 200$ GeV at RHIC [54]. Semi-inclusive yield of recoil jets with respect to associated high p_T hadron triggers was measured. Figure 6.9 depicts charged raw recoil jet spectrum for central and peripheral Au+Au collisions mea-

sured by STAR and the respective nuclear modification factor I_{CP}. The I_{CP} is nuclear modification factor defined as

$$I_{CP} = \frac{Y_{central}}{Y_{peripheral}}, \tag{6.1}$$

where $Y_{central}$ and $Y_{peripheral}$ is the yield in central collisions and peripheral collisions respectively.

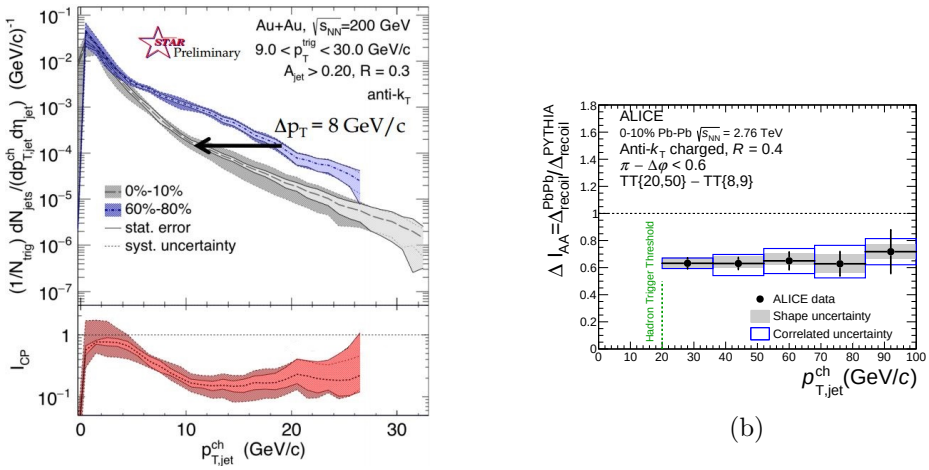

(a) (b)

Figure 6.9: (a) Charged raw recoil jet spectrum for central and peripheral collisions with I_{CP} ratio [54] (b) ΔI_{AA}, the ratio of Δ_{recoil} in Pb+Pb and p+p collisions at $\sqrt{s} = 2.76$ TeV for $R = 0.4$ [55]

We can observe significant suppression $I_{CP} = 0.2$ at $p_T > 10$ GeV/c. At low p_T, The I_{CP} is close to 1. The STAR measurement is also compared to recent measurement by the ALICE experiment at the LHC in Pb+Pb collisions. The suppression at RHIC is larger in comparison to the LHC energy at $\sqrt{s_{NN}} = 2.76$ TeV [55]. It is important to mention that analysis was performed with different measurement techniques, resolution parameter R at STAR is $R = 0.3$ and ALICE $R = 0.4$.

Figure 6.10 compares azimuthal distribution of recoil jets in peripheral and central Au+Au collisions. Significant difference in change of jet scattering angle can be seen in central collisions for $5 < p_T < 8$ GeV/c. It is subject of further theoretical study whether this difference is due to flow, background from multiple interactions or other effects.

6.3.2 Dijet imbalance

In the next recent analysis [57], the dijet imbalance A_J was measured in central Au+Au collisions at $\sqrt{s_{NN}} = 200$ GeV. A_J is an asymmetry ratio, which quantitatively characterizes the jet energy balance or imbalance. It is defined as

$$A_J = \frac{p_T^{lead} - p_T^{sublead}}{p_T^{lead} + p_T^{sublead}} \tag{6.2}$$

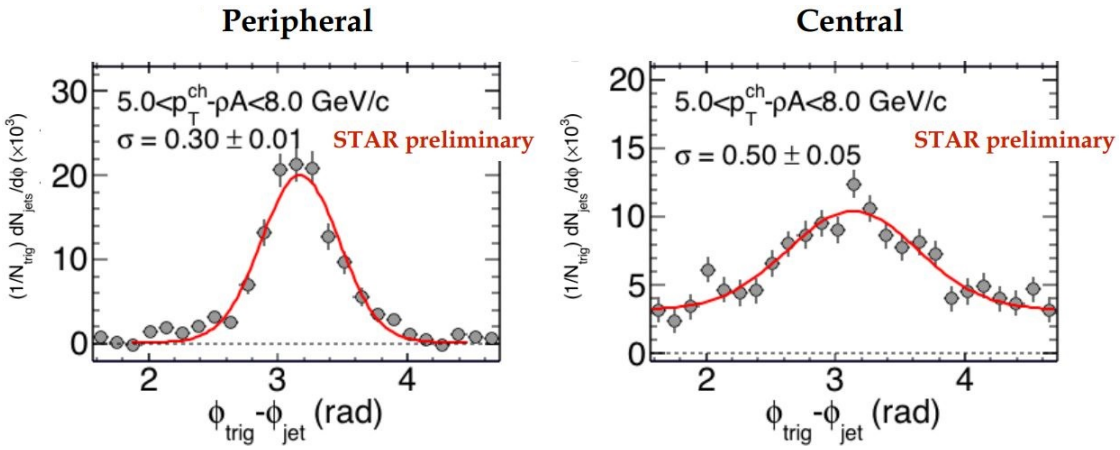

Figure 6.10: Comparison of recoil jet azimuthal distribution in peripheral (right) and central (left) collisions [56].

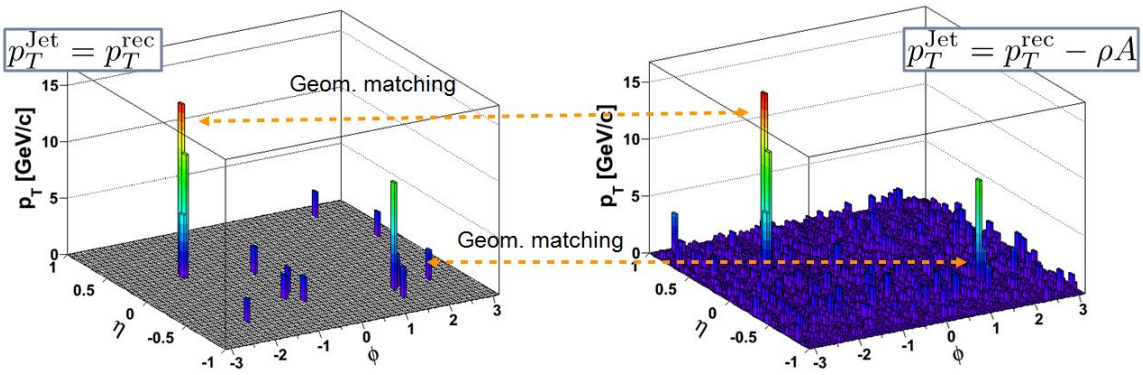

Figure 6.11: Dijet selection process with background subtraction [57].

The STAR analysis presented below focuses on focused on investigation of jet-by-jet energy loss. Results of these measurements are also used for studying jet broadening or softening. At the beginning of the analysis, dijets were selected and reconstructed by the anti-k_T algorithm with resolution parameter $R = 0.2$ and 0.4. Background and combinatorial jets were reduced by imposing a p_T cut of 2 GeV/c. The p_T cut of 20 GeV/c for leading jet and 10 GeV/c for subleading jet in angle $|\Delta\phi - \pi| < 0.4$ were applied. Then the dijet imbalance ratio was computed. This selection process of dijets can be seen in Figure 6.11.

The obtained results are depicted in Figure 6.12. The left panel shows that balance can not be restored for the p_T cut of 1 GeV/c within R=0.2. This fact is related to jet broadening. Signs of jet softening can be observed between 1-2 GeV/c, because dijets are more imbalanced above the cut $p_T^{cut} > 2$ GeV/c [57].

For the first time, the lost energy of dijets is recovered in a jet of $R = 0.4$. For smaller cone or higher constituent cutoff the imbalance however remains. On the basis of these measurements it is possible to observe jet broadening and softening.

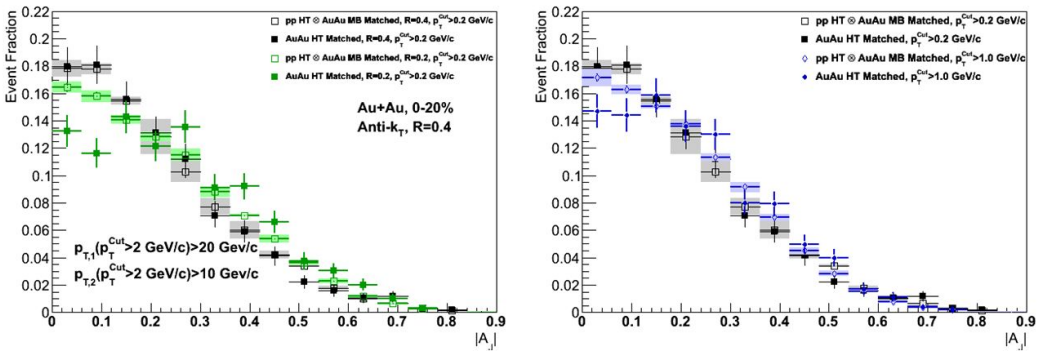

(a) (b)

Figure 6.12: Event fraction as a function of $|A_J|$: (a) jet broadening - $R = 0.2$ and $p_T^{cut} > 0.2$ GeV/c (b) jet softening - $R = 0.4$ and $p_T^{cut} > 1$ GeV/c [57].

Summary

The main subject of this bachelor thesis was to acquaint with the jet physics at RHIC, mainly with jet algorithms and their application in the study of nucleus-nucleus collisions. This work serves as my preparation for further analysis of jets in heavy-ion collisions at the STAR experiment at RHIC.

Many present particle physics experiments are focused on the research of quark-gluon plasma, which is a new state of hot and dense nuclear matter consisting of free partons. QGP is theoretically predicted by Quantum Chromodynamics that was introduced with the Standard model and briefly described in the first chapter.

QGP exists at extremely high temperature and density and it is supposed to exist in the first moments after the Big Bang. Now the production and the study of QGP is provided in laboratories by ultra-relativistic heavy-ion collisions. A nuclear collision is a dynamical process with large energy transfer which lasts only few femtoseconds. Basic kinematic observables, geometry and space-time evolution of a collision were described in the second chapter. In heavy-ion collisions, state transition of medium into QGP can occur. For probing the presence of QGP and its properties, it is necessary to have sensitive probes such as elliptic flow, suppression of high p_T particles described by nuclear modification factor and jet quenching. All of them were briefly discussed.

One of the experiments that is utilized for exploration of the behaviour and properties of the strongly interacting nuclear matter is STAR, located at RHIC in Brookhaven National Laboratory. The STAR experiment consists of several different types of subdetectors, which were discussed in the third chapter and the principle of their operation was explained. The most important detectors for jet analysis are Time Projection Chamber for charged particles and Barrel Electromagnetic Calorimeter for neutral energy. A sample of data measured by the BEMC was also presented.

The main part of this work was dedicated to jets and jet algorithms. Jets are collimated sprays of particles that are produced immediately after the collision, when partons of incoming nuclei undergo fragmentation and hadronization. Jets are studied in order to determine the properties of QGP. They can be quenched in medium that is produced in heavy-ion collisions and this phenomenon called jet quenching also helps in the research of QGP. Jet definition, jet background and jet levels are mentioned in the fourth chapter.

Jets are reconstructed from particles which energy and momentum are measured in detectors. Jet-finding algorithms are used for jet reconstruction and their main goal is to cluster a set of charged tracks and neutral energy measured by detectors into jets. The algorithm selects a set of particles, which are typically emitted close to

each other in an angle and combines their momenta to form the momentum of a jet. Jet resembles kinematic properties of the original parton therefore allows to access early stages of the collision. Jet reconstruction is successful in the p+p collisions, while in the heavy-ion collision environment is more complicated due to the large background. Ideal jet algorithm has to fulfil several attributes, for example collinear and infrared safety or fast computing time. Jet algorithms can be divided into two groups: cone and clustering. The most commonly used clustering algorithms are the k_T and the anti-k_T, which are based on selecting a starting particle and then sequentially add other particles that are close enough to the arising jet. Moreover, according to the selection of a starting particle, jet algorithms can be divided into seedless and seeded algorithms that start from the most energetic particle. The end of the fifth chapter was dedicated to the definition of an active and passive area, which are used in the process of background subtraction.

The last chapter briefly summarises some results of jet analysis at RHIC provided in recent years. There are presented measurements of jet structure, jet fragmentation, and cross section and correlation of fully reconstructed jets in $\sqrt{s_{NN}} = 200$ GeV p+p and Au+Au collisions at RHIC.

Bibliography

[1] Wikipedia, The Standart model, http://en.wikipedia.org/wiki/Particle_physics/media/File:Standard_Model_of_Elementary_Particles.svg [online 13.5.2015]

[2] F.Halzem, A.Martin, *Quarks and Leptons An Introductory Course in Modern Particle Physics*, New York: Wiley, 1984.

[3] Robert Craig Group, Measurement of the Inclusive Jet Cross Section Using the Midpoint Algorithm in Run II at CDF. Dissertation, http://www-cdf.fnal.gov/ group/WORK/DISS_PAGE/diss_page.htm [online 27.5.2015]

[4] W. Florkowski, *Phenomenology of ultra-relativistic heavy-ion collisions*. World-Scientic, Singapore, 2010.

[5] K. Yagi et al., *Quark-gluon plasma*, Cambridge University Press, 2005.

[6] The Phases of QCD, http://www.bnl.gov/today/body_pics/2010/07/phases-of-qcd-350px.jpg [online 28.5.2015]

[7] Wikipedia, Pseudorapidity, http://en.wikipedia.org/wiki/Pseudorapidity/media/File:Pseudorapidity2.png [online 26.5.2015]

[8] R. Stock, Relativistic Nucleus-Nucleus Collisions and the QCD Matter Phase Diagram, arXiv: 0807.1610v1 (2008).

[9] Sarkar, Satz, Sinha, *The Physics of the Quark-Gluon Plasma*, Springer, 2009

[10] M. Kliemant, R. Sahoo, T. Schuster and R. Stock, Global Properties of Nucleus-Nucleus Collisions, Lect. Notes Phys. **785** (2010) 23 [arXiv:0809.2482 [nucl-ex]].

[11] M. L. Miller, K. Reygers, S. J. Sanders and P. Steinberg, Glauber modeling in high energy nuclear collisions, Ann. Rev. Nucl. Part. Sci. **57** (2007) 205 [nucl-ex/0701025].

[12] C. Nonaka and M. Asakawa, Modeling a Realistic Dynamical Model for High Energy Heavy Ion Collisions, PTEP **2012** (2012) 01A208 [arXiv:1204.4795 [nucl-th]].

[13] R. Vogt, *Ultrarelativistic Heavy-Ion Collisions*, Elsevier 2007, ISBN 978-0-444-52196-5.

[14] Probing the perfect liquid with the star grid. http://www.interactions.org/sgtw/2006/1025/star_grid_more.html, 2001. [online 2.6.2015]

[15] J. Adam *et al.* [ALICE Collaboration], Measurement of charged jet production cross sections and nuclear modification in p-Pb collisions at $\sqrt{s_{NN}} = 5.02$ TeV, arXiv:1503.00681.

[16] M. Shao [STAR Collaboration], Cronin effect at RHIC, AIP Conf. Proc. **828** (2006) 49.

[17] J. Adams *et al.* [STAR Collaboration], Evidence from d + Au measurements for final state suppression of high p(T) hadrons in Au+Au collisions at RHIC, Phys. Rev. Lett. **91** (2003) 072304 [nucl-ex/0306024].

[18] L. Adamczyk *et al.* [STAR Collaboration], Jet-Hadron Correlations in $\sqrt{s_{NN}} =$ 200 GeV $p + p$ and Central $Au + Au$ Collisions, Phys. Rev. Lett. **112** (2014) 12, 122301 [arXiv:1302.6184 [nucl-ex]].

[19] X. N. Wang, Why the observed jet quenching at RHIC is due to parton energy loss, Phys. Lett. B **579** (2004) 299 [nucl-th/0307036].

[20] G. Aad et al. (ATLAS Collaboration), Observation of a Centrality-Dependent Dijet Asymmetry in Lead-Lead Collisions at $\sqrt{s_{NN}} = 2.76$â€‰TeV with the ATLAS Detector at the LHC Phys. Rev. Lett. 105

[21] D. d'Enterria, Jet quenching, arXiv:0902.2011v2, 2009

[22] Jet quenching, http://www.ellipsix.net/uploads/_9tb/atlas-jetquenching.png [online 28.5.2015]

[23] G. Odyniec, The RHIC Beam Energy Scan program in STAR and what's next ..., J. Phys. Conf. Ser. **455** (2013) 012037.

[24] K. Kajimoto, A Large Area Time of Flight Detector for the STAR Experiment at RHIC, Ph.D thesis; U. of Texas at Austin (2009).

[25] M. J. Tannenbaum, Highlights from BNL-RHIC, Subnucl. Ser. **50** (2014) 347 [arXiv:1302.1833 [nucl-ex]].

[26] K. H. Ackermann *et al.* [STAR Collaboration], STAR detector overview, Nucl. Instrum. Meth. A **499** (2003) 624.

[27] O. Rusňáková, Measurements of non-photonic electrons in STAR, Hot Quarks 2014 presentation, 2014

[28] M. Anderson, J. Berkovitz, W. Betts et.al, The STAR Time Projection Chamber: A Unique Tool for Studying High Multiplicity Events at RHIC, 2003 arXiv:nucl-ex/0301015v1

[29] M. Shao, O. Y. Barannikova, X. Dong, Y. Fisyak, L. Ruan, P. Sorensen and Z. Xu, Extensive particle identification with TPC and TOF at the STAR experiment, Nucl. Instrum. Meth. A **558** (2006) 419 [nucl-ex/0505026].

[30] M. Beddo *et al.* [STAR Collaboration], The STAR barrel electromagnetic calorimeter, Nucl. Instrum. Meth. A **499** (2003) 725.

[31] C. Yang *et al.*, Calibration and performance of the STAR Muon Telescope Detector using cosmic rays, Nucl. Instrum. Meth. A **762** (2014) 1 [arXiv:1402.1078 [physics.ins-det]].

[32] A Brief Introduction to the STAR Heavy Flavor Tracker http://rnc.lbl.gov/ jhthomas/public/HeavyFlavorTracker/ [online 12.6.2015]

[33] F.S. Bieser et al, The STAR Trigger, https://www.star.bnl.gov/public/tpc/ NimPapers/trigger/trigger_nim.pdf [online 13.6.2015]

[34] Bryan Webber, QCD Phenomenology at High Energy, http://www.hep.phy.cam.ac.uk/theory/webber/QCDlect4.pdf, [online 29.5.2015]

[35] Matteo Cacciari and Gavin P. Salam. Jet clustering in particle physics, via a dynamic nearest neighbour graph implemented with CGAL. 2006 http://www.lpthe.jussieu.fr/ salam/repository/docs/kt-cgta-v2.pdf [online 8.6.2015]

[36] Wikipedia, b-tagging, https://en.wikipedia.org/wiki/B-tagging, [online 17.7.2015]

[37] G. C. Blazey et al., Run II jet physics, hep-ex/0005012

[38] E. Bruna, ALICE/ATLAS/CMS Production and quenching of heavy flavours: pp, pA, AA comparisons" presentation on BEAUTY 2013.

[39] H. Caines [STAR Collaboration], Jet and Underlying Event Measurements in P+P Collisions at RHIC, Int. J. Mod. Phys. E **20** (2011) 1578 [arXiv:1011.4614 [nucl-ex]].

[40] G. P. Salam, Towards Jetography, Eur. Phys. J. C **67** (2010) 637 [arXiv:0906.1833 [hep-ph]].

[41] M. Cacciari and G. P. Salam, Dispelling the N^3 myth for the k_t jet-finder, Phys. Lett. B **641** (2006) 57 [hep-ph/0512210].

[42] G. P. Salam and G. Soyez, A Practical Seedless Infrared-Safe Cone jet algorithm, JHEP **0705** (2007) 086 [arXiv:0704.0292 [hep-ph]].

[43] M. Cacciari, G. P. Salam and G. Soyez, The Anti-k(t) jet clustering algorithm, JHEP **0804** (2008) 063 [arXiv:0802.1189 [hep-ph]].

[44] M. Cacciari, G. P. Salam and G. Soyez, The Catchment Area of Jets, JHEP **0804** (2008) 005 [arXiv:0802.1188 [hep-ph]].

[45] G. Soyez, Jet areas as a tool for background subtraction, arXiv:0905.2851 [hep-ph].

[46] Y. S. Lai [PHENIX Collaboration], Direct jet reconstruction in p + p and Cu + Cu collisions at PHENIX, Nucl. Phys. A **855** (2011) 295.

[47] M. Cacciari, G. P. Salam and G. Soyez, FastJet user manual, Eur. Phys. J. C **72** (2012) 1896 [arXiv:1111.6097 [hep-ph]].

[48] M. Connors, Jet-Hadron Correlations in pp and Pb-Pb Collisions with ALICE, J. Phys. Conf. Ser. **446** (2013) 012009.

[49] T. Renk, Jet correlations - opportunities and pitfalls, arXiv:1404.0793 [hep-ph].

[50] B. I. Abelev *et al.* [STAR Collaboration], Long range rapidity correlations and jet production in high energy nuclear collisions, Phys. Rev. C **80** (2009) 064912 [arXiv:0909.0191 [nucl-ex]].

[51] B. I. Abelev *et al.* [STAR Collaboration], Three-particle coincidence of the long range pseudorapidity correlation in high energy nucleus-nucleus collisions, Phys. Rev. Lett. **105** (2010) 022301 [arXiv:0912.3977 [hep-ex]].

[52] M. Ploskon [STAR Collaboration], Inclusive cross section and correlations of fully reconstructed jets in $\sqrt{s_{NN}} = 200$ GEV Au+Au and p+p collisions, Nucl. Phys. A **830** (2009) 255C [arXiv:0908.1799 [nucl-ex]].

[53] E. Bruna [STAR Collaboration], Measurements of jet structure and fragmentation from full jet reconstruction in heavy ion collisions at RHIC, Nucl. Phys. A **830** (2009) 267C [arXiv:0907.4788 [nucl-ex]].

[54] A. Schmah, Jet production in heavy ion collision at STAR, Hard Probes presentation, 2015

[55] J. Adam *et al.* [ALICE Collaboration], Measurement of jet quenching with semi-inclusive hadron-jet distributions in central Pb-Pb collisions at $\sqrt{\mathbf{s_{NN}}} = 2.76$ TeV, arXiv:1506.03984 [nucl-ex].

[56] L. Yi, STAR Overview, Hard Probes presentation, 2015

[57] K. Kauder, Di-Jet imbalance measurements in central Au+Au collisions at $\sqrt{s_{NN}} = 200$ GeV from STAR, Hard Probes presentation, 2015